JGR Planets

RESEARCH ARTICLE
10.1029/2025JE009584

Key Points:

- Machine learning is used to infer tectonic deformations from a global tectonic database
- The tectonic record indicates Mercury's global contraction is at least 6.3 km, though with substantial lateral variations
- Results indicate rapid contraction at 4.1–3.9 Ga followed by slower rates, which could mark the onset of Mercury's inner core nucleation

Supporting Information:

Supporting Information may be found in the online version of this article.

Correspondence to:

A. Broquet,
adrien.broquet@dlr.de

Citation:

Broquet, A., & Andrews-Hanna, J. C. (2026). Mercury's tectonic and geodynamic history: 1. Contractional tectonic landform analysis and tectonic strain using machine learning. *Journal of Geophysical Research: Planets*, *131*, e2025JE009584. https://doi.org/10.1029/2025JE009584

Received 4 DEC 2025
Accepted 18 MAR 2026

Author Contributions:

Conceptualization: A. Broquet, J. C. Andrews-Hanna
Data curation: A. Broquet
Formal analysis: A. Broquet
Funding acquisition: A. Broquet
Investigation: A. Broquet
Methodology: A. Broquet, J. C. Andrews-Hanna
Project administration: A. Broquet
Resources: A. Broquet
Software: A. Broquet
Supervision: A. Broquet, J. C. Andrews-Hanna
Validation: A. Broquet, J. C. Andrews-Hanna
Visualization: A. Broquet
Writing – original draft: A. Broquet

Mercury's Tectonic and Geodynamic History: 1. Contractional Tectonic Landform Analysis and Tectonic Strain Using Machine Learning

A. Broquet[1,2] **and J. C. Andrews-Hanna**[1]

[1]Lunar and Planetary Laboratory, University of Arizona, Tucson, AZ, USA, [2]Now at Institute of Space Research, German Aerospace Center, DLR, Berlin, Germany

Abstract Mercury's tectonic record is dominated by shortening landforms, including lobate scarps, high-relief ridges and wrinkle ridges. Previous analyses of these structures have used displacement–length ratios to constrain the planet's global contraction to a range of either no more than 2 km or up to 7 km. This important discrepancy has strong implications for our understanding of Mercury's geodynamic history and results from different interpretations of the tectonic record. Studies in favor of less contraction do not include wrinkle ridges and other small-scale landforms as part of the record of Mercury's contraction, while prior works arguing for large contraction are subject to greater uncertainty regarding the strain associated with individual landforms. Here we use existing mapping of tectonic landforms together with machine learning to evaluate ridge height for a more robust strain analysis. Tectonic strain is converted to global contraction considering fault orientation. Removing small secondary landforms that are parallel and in close vicinity to a primary longer landform leads to a global contraction of about 6.3 km, which is substantially higher than when neglecting wrinkle ridges (~1.2 km). Considerable global contraction is also potentially accommodated by non-tectonic means, indicating that the tectonic record underestimates the magnitude of contraction Mercury experienced. Tectonic strain exhibits prominent lateral variation, with some regions experiencing near-zero strain, while others recorded substantial deformation. Our analyses reveal a period of rapid contraction from 4.1 to 3.9 Ga at 0.02–0.04 km/Myr, followed by much lower rates of contraction, which could mark the onset of Mercury's inner core nucleation.

Plain Language Summary Mercury's surface is covered by contractional tectonic features, which are a record of planetary cooling and shrinking over time. Previous analyses of these structures have constrained the planet's global contraction to a range of either <2 km or up to 7 km. This important discrepancy has strong implications for our understanding of the interior structure and thermal evolution of the planet, as well as for the generation of an intrinsic magnetic field and the history of mantle convection. Low contraction estimates imply Mercury to have preserved substantial interior heat and required a highly insulating porous crust. On the other hand, high contraction estimates necessitate the planet to have cooled substantially and interior convection to have rapidly ceased. Here, we use existing mapping of tectonic landforms together with machine learning to revisit previous tectonic strain analyses. Our work indicates a global contraction of at least 6.3 km, which is at the high end of previous estimates. Substantial lateral tectonic strain variations are observed, implying that some regional processes have affected how the global cooling of Mercury is expressed at the surface. Our analyses reveal a non-steady tectonic strain history, which has implications for the geodynamic history of Mercury.

1. Introduction

Similar to other terrestrial planets, Mercury is covered by contractional tectonic landforms, typically classified as lobate scarps, high-relief ridges, and wrinkle ridges (Watters, 1988). These tectonic features are thought to be the record of Mercury's long history of global contraction in response to cooling of the interior and growth of a solid inner core (Knibbe & van Westrenen, 2018; Hauck II et al., 2004). Lobate scarps and high-relief ridges are long (100–1,000 km) shortening landforms with heights often exceeding 1 km. Lobate scarps are the most abundant and characterized by their asymmetric cross-section, with a steep sloping scarp face and a more gradual sloping back limb, while high-relief ridges are generally more symmetric (Watters, 1988). These landforms are generally accepted to be linked to deeply penetrating thrust faults that have recorded lithosphere-scale horizontal shortening associated with planetary cooling and contraction (e.g., Byrne et al., 2014; Di Achille et al., 2012; Watters, 2021).

Writing – review & editing: A. Broquet, J. C. Andrews-Hanna

In addition, the distribution of lobate scarps and high-relief ridges, with some following north–south trends in the equatorial regions (e.g., Watters et al., 2004), has been linked to planetary contraction during despinning (Dombard & Hauck II, 2008; Matsuyama & Nimmo, 2009) and cooling in the presence of a thinner equatorial lithosphere (Beuthe, 2010). Equatorial clusters of lobate scarps are also seen in regions with thicker crust, which is potentially due to mantle downwellings locally enhancing contractional strains (Watters et al., 2021). Lobate scarps also show a preferential orientation with respect to Mercury's large basins, indicating an important structural control of impact-induced damage zones (Klimczak et al., 2025).

Although there is a general continuum in morphology between wrinkle ridges and lobate scarps on Mercury (e.g., Loveless et al., 2024), wrinkle ridges are typically more sinuous, have lower relief (∼100 s of meters) and shorter length (20–100 km) and are mostly seen on the planet's volcanic smooth plains. Wrinkle ridges are generally interpreted as arising from folding and faulting of crustal materials above blind thrust faults, but the underlying process responsible for their formation remains uncertain. In one interpretation, wrinkle ridges and other landforms found within the smooth plains are related to deeply penetrating thrust faults and are thought to contribute to the record of Mercury's global contraction and cooling (e.g., Byrne et al., 2014; Crane & Klimczak, 2017; Peterson et al., 2020). Alternatively, wrinkle ridges and other small-scale landforms may be linked to shallowly penetrating faults resulting from the displacement of a larger nearby and primary fault or from local lithospheric flexure, and thus not be related to deep lithosphere strain and global contraction (Watters, 2021). These different considerations of the same tectonic data set naturally result in considerable discrepancies in global contraction estimates. For example, studies considering shortening landforms within the smooth plains to be related to global contraction predict Mercury's radius to have decreased by ∼7 km (e.g., Byrne et al., 2014). Alternatively, the work of Watters (2021), which considers wrinkle ridges and other small-scale landforms to be unrelated to global contraction, argues for a substantially lower contraction of at most 1–2 km. The exclusion of small-scale landforms drastically reduces the investigated sample size, thereby lowering the estimated global contraction. Using displacement–length statistics to estimate how volume change is accommodated, work by Loveless and Klimczak (2025) obtained global contraction values of 1–8 km with optimal values of ∼2–3.5 km. These values were estimated independently of sample size and did not substantially vary whether the database from Watters (2021) or Klimczak et al. (2025) was used.

The nature and penetration depth of wrinkle ridges have also been debated on other planetary bodies, and on Mars in particular. Wrinkle ridges that trace the rims of some Martian buried craters suggest thin-skinned tectonics limited to the upper volcanic units and/or nucleating at a shallow ice-rich décollement (<2 km, e.g., Allemand & Thomas, 1995; Mangold et al., 1998; Karagoz et al., 2022). In contrast, a systematic difference in ridge spacing between the northern lowlands and southern highlands may be related to differences in crustal and lithosphere thickness and suggest lithosphere-scale faulting (Montési & Zuber, 2003). Importantly, the presence of wrinkle ridges on Mars where flexural stresses should be tensile supports a link to global contraction and compressional stresses (Andrews-Hanna & Broquet, 2023). Models using wrinkle ridge topography have been used to argue in favor of both thin- (e.g., Watters, 2004) and thick-skinned (e.g., Andrews-Hanna, 2020; Loveless et al., 2025; Okubo & Schultz, 2004) tectonics. One clear terrestrial analog to wrinkle ridges is the Yakima fold and thrust belt. Structural modeling indicates thrust faults in the Yakima Fold Province to extend to ∼4–8 km décollement levels, well below the upper volcanic units (Crane & Klimczak, 2019a), which is more consistent with thick-skinned tectonics.

The different interpretations of Mercury's tectonic record and associated cooling history have profound implications for the thermal evolution of the planet (e.g., Tosi et al., 2013), the generation of a geodynamo (Johnson et al., 2015) and the history of mantle convection (Michel et al., 2013). A key outstanding question is to what extent strain from deformation of the lithosphere contributes to the tectonic record. While some previous studies have investigated deformation processes such as from mascon loading (Kennedy et al., 2008), cooling of volcanic units (Freed et al., 2012), and mantle flow (James et al., 2015; Watters et al., 2021), no systematic comparisons have been made between the tectonic record and lithosphere deformation patterns constrained by observed gravity and topography. In addition, due to limitations in existing techniques, previous studies have only investigated in detail a subset of the tens of thousands of shortening landforms in detail (e.g., Byrne et al., 2014; Loveless et al., 2025; Watters, 2021). The measured ratio between the tectonic displacement and fault length (a displacement–length scaling relationship) was then used to estimate global contraction. However, the appropriateness of this approach for a global tectonic database, in which a single structure may be subdivided into multiple separate features, and which is subject to fault linkage and observational gaps, remains unclear.

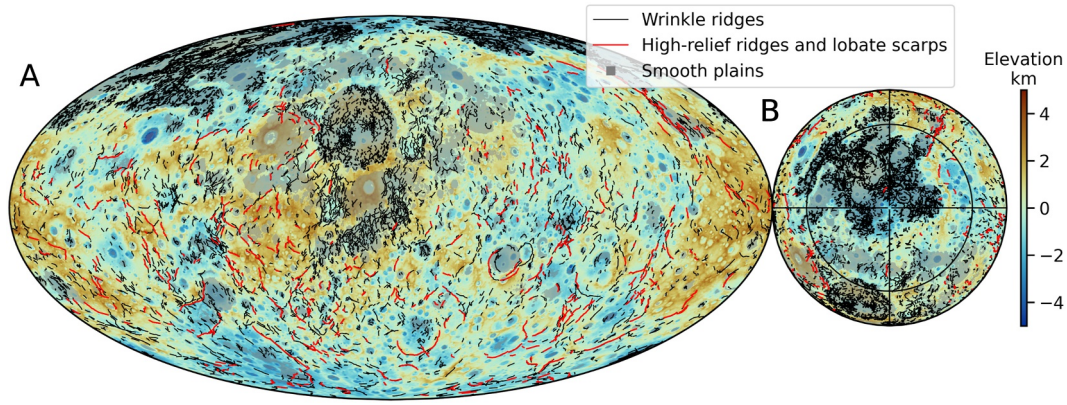

Figure 1. Mercury's tectonic record. Mollweide (a) and north polar (b) projections of elevation data displaying wrinkle ridges, high relief ridges and lobate scarps (Klimczak et al., 2025; Watters, 2021), together with smooth plains (Denevi et al., 2013).

The present paper is the first of a set of two that provides constraints on Mercury's tectonic and geodynamic history. In this first paper, we revisit Mercury's deformation history by investigating the global population of tectonic landforms, as mapped by Klimczak et al. (2025) and Watters (2021). We make use of machine learning to delineate the extent of the ridges orthogonal to their length in order to measure heights and evaluate tectonic strain at each location. We present a tectonic strain model using only the primary tectonic structures, defined as the longest structure along one principal direction within a narrow region, excluding smaller adjacent structures. Although these approaches do not consider the geological context of each landform in detail, they provide important information on global tectonic catalogs containing thousands of landforms, and prevent overestimating strain from double counting of ridges while considering wrinkle ridges as contributing to Mercury's global tectonic strain. Tectonic strain is related to global contraction, taking into consideration the distribution and orientations of ridges. In the second paper, we invert observed gravity and topography to estimate the contribution of lithospheric membrane–flexural strains to the tectonic record. Two compensation mechanisms are investigated and include either crustal loading only or a combination of mantle support and isostatic compensation at long wavelengths with shorter wavelengths dominated by crustal loading. Together, these papers provide new insights on Mercury's tectonic history, with implications for the geodynamic evolution of the planet.

2. Methods

2.1. Constructing a Shortening Landform Profile Database

Recent geologic mapping by Klimczak et al. (2025) has shed light on Mercury's tectonic record. In that work, 18,450 individual tectonic segments have been mapped, building upon previous tectonic databases (Byrne et al., 2014, 2018; Crane & Klimczak, 2019b; Klimczak et al., 2012). We note that illumination bias from MESSENGER could slightly affect the inferred distribution of landforms in this catalog (e.g., Byrne et al., 2014). Among these, 9,845 individual segments are denoted as shortening landforms and have a cumulative length of ∼500,000 km (Figure 1). The majority of mapped landforms correspond to wrinkle ridges (∼88% by length, or 440,000 km), which are concentrated in Mercury's smooth plains. These plains, which cover ∼27% of the surface (Denevi et al., 2013), are thought to be of volcanic origin and to have been emplaced after the Caloris impact basin formed (∼3.7 Ga; Orgel et al., 2020), making them markedly younger than the surrounding cratered terrains (∼4.0–4.2 Ga; Head et al., 2011). We note that broad anticlines lacking a clear tectonic rupture at the surface, such as those mapped in Crane and Klimczak (2017), are not part of this tectonic inventory. Following previous work, we treat the ridges associated with tectonic landforms as arising from displacement along a simple fault at depth to calculate strain (e.g., Byrne et al., 2014), though the actual tectonic geometry likely would have involved a more complex geometry of faults and folds (e.g., Loveless et al., 2025). For simplicity, in the following text, shortening landforms will be referred to as ridges.

Given the vast number of tectonic structures on Mercury, most previous studies have relied on relief measurements of a small subset of the population and then applied the derived displacement–length scaling relationships to the global population (e.g., Byrne et al., 2014; Watters, 2021). However, it is unclear whether these scaling

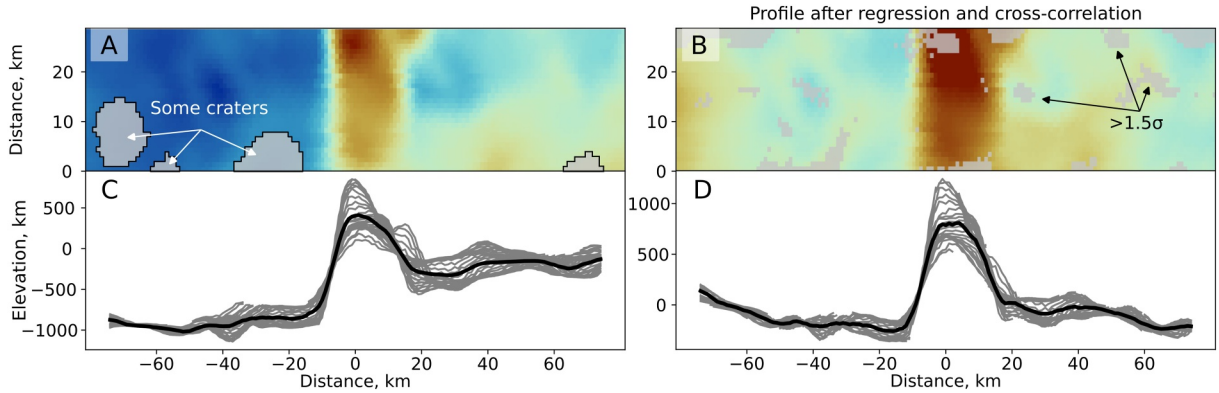

Figure 2. Ridge profile extraction approach. Stack of extracted profiles (a), and stack after linear regression, cross-correlation, and removal of the regional slope (b). Grayed regions indicate large craters in (a) and locations with elevation >1.5 standard deviation (σ) away from the local mean in (b) Elevation profiles from (a, b) with the average in black (c, d). The final retained profile for this ridge segment is the average black profile in (d).

relationships are appropriate for estimating tectonic strain from a global tectonic database. In particular, segmentation either due to the sparse topographic expression of a ridge, subdivision during the mapping, or fault linkage (e.g., Cartwright et al., 1995; Schultz, 1999), will lead to the existence of short segments with high relief. In that case, the use of displacement–length ratios (based on completely mapped ridge segments) would substantially underestimate the true height of the shortening landform, the associated fault displacement, and the tectonic strain at that location. Numerical simulations of extensional fault patterns have also shown that small-scale and random rock strength heterogeneity can substantially affect fault size-frequency distribution, which implies that extrapolated scaling relationships are subject to large uncertainties (Hardacre & Cowie, 2003). Rather than using displacement–length ratios, we here use a global database of tectonic structures together with a global Digital Elevation Model (DEM) in order to generate average profiles perpendicular to each ridge, and use a machine learning algorithm to extract the ridge width and height from those profiles.

In order to analyze shortening landforms and estimate tectonic strain, we extracted elevation profiles orthogonal to each contractional feature of the tectonic catalog of Klimczak et al. (2025). Elevation profiles are derived from a global stereo DEM (Becker et al., 2016), with spatial resolution of 665 m per pixel at the equator (though with substantial variations in true resolution; see below). To ease the extraction of profiles orthogonal to the ridge azimuth, each of the 9,845 individual arcuate ridge polylines was first simplified into straight subsegments, with new subsegments created each time the azimuth changes by more than 20°, resulting in 53,085 subsegments. This numerical subdivision allows for a more adequate extraction of elevation profiles orthogonal to arcuate landforms. Elevation profiles orthogonal to each straight subsegment are then extracted every 1 km along the strike (Figure 2) and stored for further analyses. The profiles extend to 70 km on either side of the ridge crest, which is sufficient to account for the widest tectonic landforms. The individual profiles from one ridge subsegment are detrended, shifted and aligned to maximize the cross-correlation between each profile and an average of all profiles for that ridge subsegment (Figure 2, see also Andrews-Hanna, 2020). Elevations >1.5 standard deviations away from the mean value for that location along the profile are excluded from the analysis. This approach allows the construction of a representative average ridge profile for each subsegment, while excluding impact craters smaller than the investigated landform and other non-tectonic features, provided they don't statistically significantly affect the regional topography. Large crater rims that parallel a fault can introduce errors in the ridge mapping, but this should have a small effect on our overall analysis of tens of thousands of segments. This procedure is applied to the entire subsegment database in order to extract representative average ridge profiles across Mercury's surface.

We note that although data from Mercury Laser Altimeter (MLA) may provide better resolved elevation data in the northern hemisphere (Zuber et al., 2012), variations on the order of tens of meters would have little effect on our global strain estimate. Importantly, MLA provided only sparse measurements in the southern hemisphere, and thus, analyses of topography data there necessitate the use of the stereo DEM. To evaluate the scale-dependence of the error in the stereo DEM, we computed the Fourier power spectrum of identical swaths in the MLA data and the DEM in the northern hemisphere. The error is found to reach 20% at a half-wavelength resolution of 27 km

and 50% at a half-wavelength of 9 km (the limiting useful resolution of the data, Figure S1 in Supporting Information S1). Similarly, we show that the topography of a ∼100-km-diameter crater in the southern hemisphere in the stereo DEM matches that of a similarly sized crater in the northern hemisphere in the MLA data. These tests support the analysis of ridges with widths greater than several 10's of km, with at least partial recovery of details of the structure at scales of ∼10 km (see also Nishiyama et al., 2026). While some individual ridge profiles may be subject to measurement errors, in the case of no systematic bias, random errors in our topographic profiles are expected to average out when assessing global strain estimates using tens of thousands of ridge profiles. This analysis also shows that smoothing of topography from the DEM will lead to the overestimation of the width of tectonic landforms and the underestimation of their relief and associated displacement and strain. Thus, all contraction estimates provided in this work should be regarded as lower bounds.

2.2. Delineation of Shortening Landforms Using Machine Learning

To assess the height of a landform, one must know where it begins and ends in the profile orthogonal to the strike, in order to define the elevation of the surrounding surface to which the ridge crest is compared. Given the substantial variability in the background topography, this determination of the ridge end points is not trivial. Here, we define the ridge end points as the beginning and end of the ridge in the average profile taken orthogonal to the ridge strike, which together define the ridge width. We utilize a deep convolutional neural network (Krizhevsky et al., 2012) to map such end points in our profiles and extract characteristics across the entire shortening landform population. The essence of this approach lies in building and training a neural network to find the optimal set of conditions that link an input elevation profile to the delimitation of its central tectonic landform. Both a training and testing data sets are constructed, each based on 88 visually evaluated profiles scattered across the surface and for which we have identified points that belong to the ridge and the corresponding end points. As shown below, and because the mathematical relationships for this 1D recognition problem are simple, our training data set is sufficient to map shortening landforms with good accuracy.

The neural network is constructed using the Keras application programming interface for TensorFlow (Abadi et al., 2016) and is trained using as input the 88 height-normalized (from 0 to 1) profiles and as output 88 manually created binary masks locating the ridge in the profile of our training data set. We note that input data normalization is a common pre-processing procedure in machine learning and improves the network's overall efficiency. Performance is evaluated using a binary cross-entropy loss function (which is adequate for binary classifications) on the test data set that the network has not encountered during prior training sessions. The final layer of the neural network is designed to output, for each point in the profile, a probability of being part of the ridge. We optimize the network's architecture, encompassing the connections and numbers of layers as well as the proficiency in ridge recognition (known as hyperparameters), using the Hyperband hyperparameter sampling algorithm (Li et al., 2018). The parameter space search method has no influence on the results of this task.

As a post-processing step, the output probability distribution is fitted by a boxcar to allow for the binary extraction of the ridge profile. The best neural network model consists of two densely connected layers with 384 and 512 neurons and can locate ridges with remarkable accuracy (Figure 3, Figures S2 and S3 in Supporting Information S1). Once trained, the neural network is applied to the global population of tectonic landforms to extract from our 53,085 average subsegment profiles the central ridge within its margin. We acknowledge that this automated landform mapping approach might be susceptible to uncertainties in elevation data or small-scale variability in ridge profiles. However, these statistical errors would largely diminish over tens of thousands of analyzed profiles and have minimal effect on the total investigated strain. Below, we also discuss and validate our automatically estimated heights compared to previous work.

2.3. Morphology of Shortening Landforms

The morphology of a tectonic structure can provide information on its mode of formation (e.g., Andrews-Hanna, 2020). Because two ridges of different height and width may have a similar morphology, the extracted ridge profiles between their end points are rescaled to a constant width using a linear transformation in which the proportions are preserved. When required, extracted ridge profiles are flipped in order for all ridges to face the same direction, depending on their vergence. Because height dominantly affects the profile of a ridge, ridge elevations are normalized from 0 to 1. We then classify ridges based on their morphology using a K-means partitioning algorithm (MacQueen, 1967). The optimal number of classes is estimated based on a silhouette

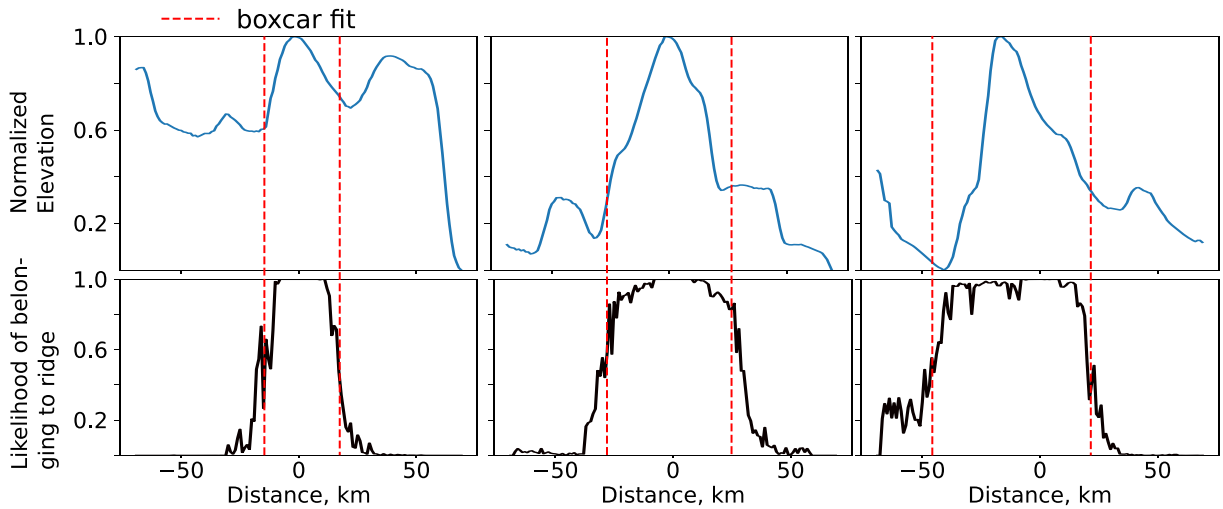

Figure 3. Normalized ridge elevation (top) and likelihood of belonging to the ridge as given by the neural network (bottom). The red dashed line shows the boxcar fit and delimits the selected ridge end points that are selected. These profiles have not been seen during prior training sessions.

criterion (Rousseeuw, 1987). Rather than relying on descriptive classification or neglecting distinctions between the different types of landforms, this algorithm mathematically groups landforms with similar shapes across Mercury's surface.

2.4. Shortening Landform Categories in the Global Tectonic Catalog

In the database of Klimczak et al. (2025), shortening landforms are not categorized into wrinkle ridges, lobate scarps, and high-relief ridges. This lack of subdivision reflects the continuous gradation observed among landform types, which complicates their discrete classification. For example, a study by Loveless et al. (2024) found no statistical difference in morphology between lobate scarps and wrinkle ridges. Nevertheless, differences in morphology, formation mechanism, and underlying cause between the populations of lobate scarps and wrinkle ridges have contributed to the different interpretations of Mercury's strain history (e.g., Watters, 2021). In addition, the ridge line segments reported in the database of Klimczak et al. (2025) and Watters (2021) are not identical, implying that one-to-one comparisons are not straightforward. Therefore, to categorize individual landforms in the global catalog of Klimczak et al. (2025), we compared the location, azimuth, and length of each segment to the lobate scarp and high-relief ridge mapping of Watters (2021). This approach allowed us to extract, from the global catalog of Klimczak et al. (2025), features not present in the high-relief ridges and lobate scarp mapping of Watters (2021). Under the assumption that the majority of the global population of lobate scarps and high-relief ridges are mapped in Watters (2021), most of the remaining features in the catalog of Klimczak et al. (2025) would be wrinkle ridges.

Below, when discussing all ridges, we refer to all landforms mapped by Klimczak et al. (2025). Lobate scarps and high-relief ridges are those mapped in Watters (2021). Wrinkle ridges are extracted from the ridge database of Klimczak et al. (2025) using the approach described above, though we note again that Klimczak et al. (2025) do not separate structures into categories. This classification has little implications for the main results of this work, which focus on the estimation of global contraction and tectonic strain variations.

2.5. Primary Landform Selection

One important consideration when estimating tectonic strain is the origin of individual tectonic structures. In some previous work, an independent fault was attributed to each tectonic landform, including small scarps on the shoulder of a larger shortening landform (e.g., Byrne et al., 2014; Crane & Klimczak et al., 2019b). When evaluating the strain from a population of landforms, this approach can lead to errors as it can cause double counting of the strain from one landform when it is in close proximity to another (Watters, 2021). For example, a single primary fault at depth may be responsible for a given landform, but may be associated with multiple faults and fractures at the surface. In the work of Watters (2021), groups of nearby and parallel tectonic structures were

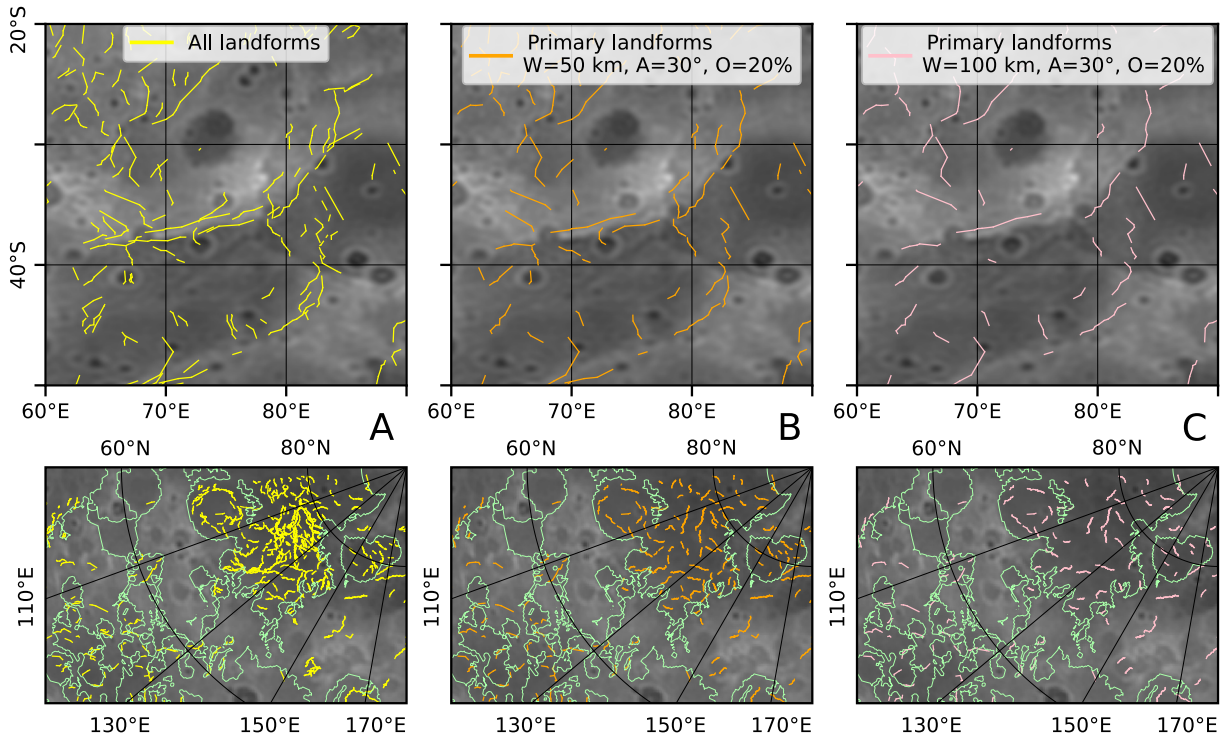

Figure 4. Regional comparison of all landforms (a) to our automated primary ridge selection (b, c) in the cratered terrains (top) and in the smooth plains (bottom). The box widths (W), the allowed azimuthal deviation (a), and the maximum overlap fraction (O) for primary ridge selection are provided in the legend (see text for details). For the geologic context, smooth plains are outlined in light green, and a greyscale topography map is shown.

linked to a single primary fault. This consideration results in considerably smaller estimated tectonic strains compared to the approach that attributes an independent fault to each tectonic landform. Similarly, in our automated ridge height extraction algorithm, the same topographic profile and height may be assigned to multiple close parallel structures in the database. This will multiplicate our inferred tectonic strain, implying that the catalog of tectonic landforms must be revised for our purposes. While using all landforms may overestimate strain, grouping nearby but unrelated faults might also underestimate strain. Given the importance of this consideration for tectonic strain, we here explore different criteria to select primary landforms and exclude nearby shortening structures linked to the deformation of the primary.

To map primary structures, we first created a rectangular box centered along each ridge segment, the width of which was kept as a free parameter (nominal width, $W = 50$ km). As all segments have been preliminarily divided into straight subsegments with an allowed azimuthal variability of 20°, this approach also works for arcuate landforms. A landform is considered as primary either if it is not intersecting any other box including parallel landforms (nominal maximum azimuth deviation allowed, $A = 30°$) over more than a given fraction of the rectangular box area (nominal overlap fraction, $O = 20\%$), or if it does intersect such boxes but is the longest of all (see Figure S4 in Supporting Information S1). This approach effectively removes small secondary shortening landforms that are parallel and in close proximity to a longer one, and intrinsically assumes that the removed structures are related to the single primary fault that formed the longest landform in that region and specific direction.

The most important parameter in the selection of primary landforms was found to be the width of the rectangular box along each segment (Figure 4). A reasonable lower limit for this parameter would be 50 km, which is about the average width of shortening landforms on Mercury (see below). Using this parameter ensures that only small-scale shortening landforms on the shoulder of a larger one are excluded, thereby limiting the effect of double counting on strain estimates. Rather than using a constant box width, an alternative approach would have been to scale the box width as a function of the local strain, as larger strains are expected to be accommodated over larger areas. However, the manual or geologic segmentation of landforms in the database substantially affects the inferred local strain and would bias such an approach. For that reason, we here opted for a constant box width. We

find that the simple approach of a constant choice in W performs well in most instances. While the optimal choice of the rectangular box width, overlap fraction, and maximum allowed azimuth deviation, may vary depending on the particular structures and settings considered, the above nominal parameters ($W = 50$ km, $A = 30°$, $O = 20\%$) were found to provide a reasonable primary mapping that compares favorably to the primary fault identification discussed in Watters (2021) (see Figure 4 and compare to Figures S1 and S2 in Supporting Information S1 Watters, 2021). We note that, in the case of ridge segmentation or ridges being expressed en échelon with >20% overlap, our approach would underestimate regional strain as only the longest regional ridge would be kept for further analysis. Similarly, by allowing up to 20% of overlap, this approach has the potential to overestimate strain by 20% in the case of overlapping ridge segments.

We emphasize that this primary landform selection approach is purely geometric and does not rely on detailed structural geologic mapping. However, the prime objective of the approach is to correct for the multiple counting of strain when multiple polylines are associated with a single shortening structure, which is frequent in the tectonic catalog of Klimczak et al. (2025) (Figure 4). In addition, this approach assumes that nearby and parallel landforms contribute to the relief of a single primary landform, which is present only once in the primary landform database. For two nearby and parallel faults, a synchronous record of strain is likely. Thus, we deem asynchronous fault displacements in the same fault family to be rare and since elastic strain adds linearly regardless of timing, asynchronous activity would not introduce errors to our analyses. For completeness, contraction and strain parameters are given when considering all landforms and for different primary selection criteria.

2.6. Tectonic Strain and Planetary Contraction

The height, length, and azimuth of a shortening landform can be used to infer the magnitude and direction of the tectonic strain (ε). Here, we only evaluate the dip-slip component responsible for the ridge height, though we note that some faults show oblique-slip trends (i.e., Galluzzi et al., 2015). We define tectonic strain as the areal strain or the fractional change in area computed by summing the inferred horizontal displacements scaled by the associated landform segment lengths and dividing by the area in which they are contained. The strain can then be linked to shortening and global contraction or radius change. Two extreme scenarios can be used to describe how shortening is related to global contraction depending on the organization of ridges and associated faults.

In one extreme scenario of a set of parallel faults, tectonic strain only releases the shortening in one direction, the areal strain is equal to the linear strain, and the planetary radius change (ΔR) is simply equal to horizontal areal strain times radius, $\Delta R = \varepsilon \times R$ (under the assumption of small strain). This approach is appropriate when investigating organized fault systems, such as the circumferential pattern of faults around Tharsis on Mars that shows little evidence of strain release in the orthogonal direction (e.g., Andrews-Hanna & Broquet, 2023). However, in this scenario, shortening in the perpendicular horizontal direction does not get released by faulting, and instead may result in the buildup of elastic strain, the non-tectonic release of strain, or may be countered by pre-existing strains in the lithosphere (e.g., from flexure).

In the other extreme limit of a set of faults in orthogonal directions, areal strain is recorded equally in all directions, and the radius change is estimated as $\Delta R = R \times \varepsilon/2$ (in the limit of small ε). This assumption provides a strain estimate equivalent to the formulation in Watters (2021), and was used by most previous studies of Mercury's global contraction (e.g., Byrne et al., 2014; Di Achille et al., 2012). However, both approaches assume that all shortening is expressed in the tectonic record, and do not consider the possibility for strain to be accommodated by other means such as pore compaction, elastic compression not exceeding the yield strength of the crust, or small-scale failure (e.g., Andrews-Hanna & Broquet, 2023; Klimczak, 2015). In addition, while wrinkle ridges are mostly disorganized in the smooth plains, some clear structure with a predominant north–south orientation is seen for lobate scarps and high-relief ridges (Figure 1). There is no evidence that this unidirectional strain is offset by faults in the opposing direction in other regions.

These two extreme cases lead to a factor 2 difference in the estimated global contraction. As is often the case, the ideal approach might lie between these two extremes, which implies that previous work might have substantially underestimated global contraction from tectonic strain. Here, rather than making assumptions on the direction of strain release, we estimate the linear strain considering ridge azimuths normalized to range from 0 to 180° and using 10° azimuth bin width. For an azimuth A_z, we evaluated the maximum (ε_1) and minimum (ε_2) linear strains at A_z and $A_z + 90°$. The total radius change for that azimuth is estimated as $R \times (\varepsilon_1 - \varepsilon_2/2)$ and the global contraction is estimated by summing shortening in all directions. This approach allows the release of strain in all

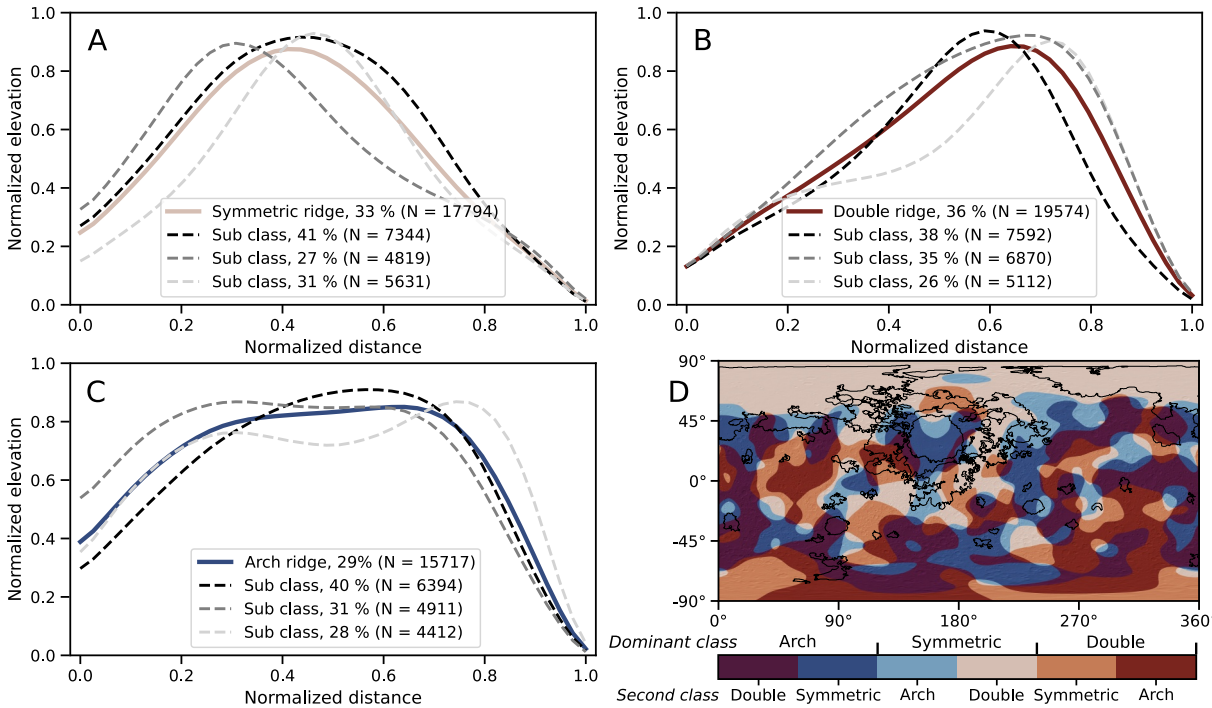

Figure 5. Results from a K-means classification for 3 main ridge classes, symmetric (a), double (b), and arch (c), with associated 3 sub-classes. Distribution of the ridge class across Mercury's surface (d). The color scale indicates both the most and second to most abundant classes per area. A black contour of major smooth plain units is added for the geologic context. Example ridge profiles are provided in Figure S5 in Supporting Information S1 and a global image with class-colored ridges is shown in Figure S6 in Supporting Information S1.

directions and recovers the strain formulation for parallel ($\varepsilon_2 = 0$; $\Delta R = R \times \varepsilon_1$) and orthogonal ($\varepsilon_1 = \varepsilon_2$; $\Delta R = R \times \varepsilon_1/2$) landforms. For an isotropic global contraction leading to the formation of randomly oriented landforms, we obtain $\Delta R = R \times \varepsilon_1/2$, equivalent to the radius change formulation found in the literature in the limit of small ε (e.g., Byrne et al., 2014; Watters, 2021).

This new strain analysis approach will increase the global strain and radius change contribution of organized tectonic features, such as the north–south trending lobate scarps and high-relief ridges, and decrease that of randomly oriented landforms, such as wrinkle ridges in the northern smooth plains. The shortening is calculated assuming a 30° fault dip (e.g., Byrne et al., 2014; Pegg et al., 2021; Watters, 2021) and translated into map form using a circular 400-km-wide moving window. We note that the size of the moving window determines the area where the two shortening components, ε_1 and ε_2, are estimated, which will affect the inferred contraction. In general, for a small window, fewer landforms contribute to releasing strain in the direction orthogonal to the dominant tectonic fabric (i.e., ε_2 decreases) and this will increase the estimated areal contraction. This effect is further discussed in Section 3.4.

3. Results

3.1. Morphology of Shortening Landforms

For our K-means analysis of ridge morphology, choosing 3 main ridge classes was found to maximize the silhouette criterion. Increasing the number of classes led to individual ridge classes having similar silhouettes. Interestingly, the 3 main ridge classes that are recovered resemble those discussed in Andrews-Hanna (2020) for Martian wrinkle ridges, and include a symmetric ridge class (33%, $N = 17{,}794$, Figure 5a), a double ridge class (36%, $N = 19{,}574$, Figure 5b), and an arch ridge class (29%, $N = 15{,}717$, Figure 5c). The symmetric ridge is characterized by similar slopes on the opposing ridge flanks with no clear vergence direction and is interpreted as arising from nearly symmetric thrust and backthrust faults. Double ridges present a steep forelimb and a broad backlimb with a secondary inflection, and are interpreted as resulting from a dominant thrust and a subsidiary antithetic back thrust. Arch ridges display a broad concave downward flank with an opposing steep flank. For

information on the variability within each class, the ridge population among each class is also subdivided into 3 subclasses. The moderate variability amongst ridge sub classes indicates that the main classes are well defined, though we note that some ridge sub classes resemble each other (Figure 5). As expected, the average profile across the entire class is smoother than the subclasses, and the average subclass profiles tend to be smoother than the typical average profiles across individual ridge segments (Figure S5 in Supporting Information S1).

We found no clear correlation between ridge morphology and height or between ridge morphology and length. The same ridge morphologies and associated distribution were found when analyzing either wrinkle ridges only or lobate scarps and high-relief ridges only. Ridge morphology was also found to strongly vary along individual ridges, with ridges varying from symmetric to double or double to arch over tens of kilometers length scales, as is the case on Mars (Andrews-Hanna, 2020). We have also considered the spatial distribution of the ridge class across Mercury's surface. The spatial density of each ridge class was computed, and the most and second to most abundant ridge classes were color-coded (Figure 5d, see also Figure S6 in Supporting Information S1). Wrinkle ridges in Mercury's northern smooth plains are dominantly found to be either symmetric or double, while ridges within the Caloris basin generally resemble the arch or symmetric class. In the cratered terrains, the dominant ridge classes are arch and double ridges (darker colors). Thus, as with Mars, we find substantial variability in profile both between and within ridges. While the variability in the profiles likely reflects the local arrangement of faults in the subsurface, it does not introduce any systematic effects into our global analysis of strain.

3.2. Length, Height, and Width of Shortening Landforms

In addition to ridge length, which can be directly extracted from the catalog of Klimczak et al. (2025), our neural network mapping approach determines ridge height and width for each average ridge profile in our database of 53,085 ridge subsegments. Ridge height is measured as the peak ridge height in the extracted profile minus the average height of the two ridge end points. Ridge width is estimated using the distance between the two opposing ridge end points. We have compared our automatically derived ridge heights to manual mapping done in Watters (2021) and found an excellent agreement (Figures S2 and S3 in Supporting Information S1).

We note that we observed a few cases of overestimated ridge height, in particular for wrinkle ridges located on a broader topographic scarp or crater rim, but this effect is minimal for the global population and is likely balanced by underestimated heights in cases of ridges adjacent to a scarp or crater rim. Various tests indicated that the most relevant parameters affecting the ridge height and inferred tectonic strain are (a) the maximum allowed offset between the mapped tectonic segment and the ridge delimitation and (b) the boxcar fit to the probability of belonging to the ridge inferred by the neural network. The effect of varying these parameters on the estimated global contraction is discussed in Section 3.4 below. Finally, we note that the global DEM used in this work smooths topography at the scale of some investigated landforms. This smoothing effect leads to an underestimation of the ridge height and an overestimation of the ridge width.

Importantly, our automated ridge analysis approach allows efficient estimation of the average ridge height at multiple locations along a ridge segment for thousands of ridges. Therefore, this method improves upon studies that used displacement–length scaling relationships and only considered the maximum height along ridges spanning hundreds of kilometers, thereby establishing an upper limit on tectonic strain (e.g., Watters, 2021). In addition, our approach naturally corrects for the possible tapering of the fault displacement toward the end points in the along-strike direction (Mège & Riedel, 2001), as the average ridge height is directly estimated there.

The average and standard deviation of the length of lobate scarps and high-relief ridges, as mapped in Watters (2021), is found to be ~95 ± 85 km, with no clear difference between the average lengths of high-relief ridges and lobate scarps (~115–93 km, respectively). Note that the width, length, and height of tectonic landforms are found to nearly follow normal distributions (Figure 6). For these landforms, the average ridge length is two times greater than the average ridge width of ~40 ± 12 km. The average height of these tectonic landforms is found to be ~650 ± 315 m, with no statistically meaningful difference in height between lobate scarps and high-relief ridges. Note that while the spread in ridge width is relatively small, ridge height and length vary substantially across the lobate scarp and high-relief ridge database of Watters (2021). We found that ridge height is weakly correlated and increases with ridge width (Pearson coefficient: 0.38; p-value <0.001) and surprisingly weakly correlated with ridge length (Pearson coefficient: 0.17; p-value <0.001). A weak correlation is at odds with previous work as well as with the expectation that a longer ridge should be associated with a greater relief (e.g., Watters, 2021), and indicates that factors other than ridge length as determined from the database exert a stronger control on ridge

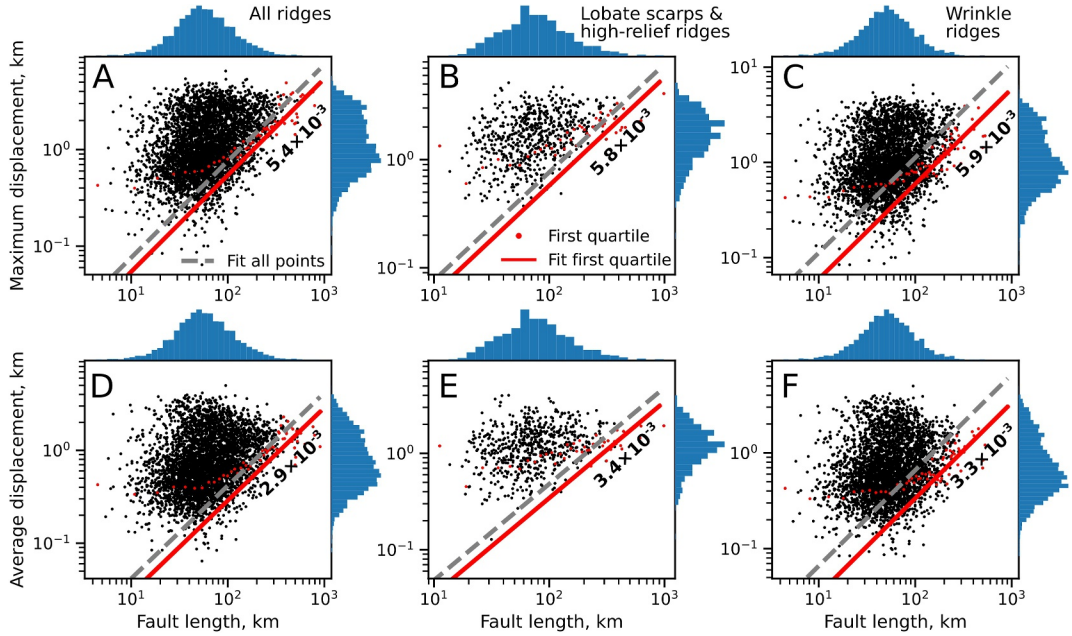

Figure 6. Fault length versus maximum (a–c) and average displacement (d–f) for all primary ridges ($N = 9{,}845$; (a, d) and for primary lobate scarps and high-relief ridges ($N = 645$; (b, e) and wrinkle ridges ($N = 9{,}200$; (c, f). Histograms are appended to each axis to help visualize the data spread. The solid red line indicates the best-fit linear trend to the first quartile, and the dashed gray line shows the best-fit to all points. Red dots indicate the first quartile of the displacement for each of the 100 length bins. Considering all landforms, and not only our defined primary ones, provides similar results, as shown in Figure S7 in Supporting Information S1.

height. This observation highlights the importance of incomplete mapping, subdivision of continuous ridges in the database, ridge segmentation and destruction, as well as other processes that will subsegment a ridge in the lobate scarp and high-relief ridge database. Note that similar results are obtained when analyzing segments identified as lobate scarps and high-relief ridges in the catalog of Klimczak et al. (2025). Thus, although the proportionality of displacement with fault length is a robust physical phenomenon rooted in the physics of elasticity and fault growth, the application of displacement–length relationships to large catalogs of planetary structures should be undertaken with caution, if at all. Further discussion on this point is provided in Section 3.3.

When considering wrinkle ridges only, we obtain average lengths and widths of ~45 ± 35 km and 18 ± 7 km, respectively. As expected, the average height of wrinkle ridges of 350 ± 290 m is smaller than for high-relief ridges or lobate scarps. In general, wrinkle ridges on Mercury have higher heights than on the Moon (~200 m) or Mars (~100 m), which might be related to Mercury having experienced a greater amount of global contraction (see Andrews-Hanna, 2020; Schleicher et al., 2019). Again, a weak positive correlation was found between wrinkle ridge length and height (Pearson coefficient: 0.23 < 0.001). Both the length–width ratio as well as the weak correlation between ridge length and height demonstrate that most wrinkle ridges are segmented in the database.

Ridge heights can be associated with a fault displacement and horizontal shortening when assuming a fault dip angle. Fault dips are expected to vary substantially with depth, depending on the local tectonic regime and properties of the crust. Previous works have shown that dip angles can vary from 10° to 50° (e.g., Galluzzi et al., 2015, 2019; Loveless et al., 2025; Pegg et al., 2021; Sibson & Xie, 1998), while others have assumed dip angles of 25–35° (e.g., Byrne et al., 2014; Watters, 2021). On Mars, despite the diversity of tectonic architectures associated with wrinkle ridges and variability in dip near the surface, assuming a 30° dip for large populations is a reasonable approximation (Andrews-Hanna, 2020). Over large populations of faults, the variability between individual structures should average out. When considering all tectonic landforms (i.e., wrinkle ridge, high-relief ridge, and lobate scarp, $N = 9{,}845$) and a fault dip angle of 30°, fault displacements have an average and standard deviation of 0.77 ± 0.60 km. This value is lower than for lobate scarps (1.29 ± 0.63 km, $N = 581$) or high-relief ridges (1.30 ± 0.56 km, $N = 64$), but higher than for wrinkle ridges only (0.72 ± 58 km). We note that a shallower dip of 20° would lead to the prediction of a ~40% lower displacement when compared to a dip of 40°.

3.3. Displacement–Length Relationships for Shortening Landforms

In an ideal tectonic and observational setting, longer ridges are expected to be associated with greater displacement along their faults and thus have greater heights. However, as discussed above, several processes may bias this relationship, leading to the existence of short ridge segments with high relief. For example, fault linkage will cause the fault to be expressed as en échelon short ridge segments (Cartwright et al., 1995). In addition, incomplete ridge mapping as well as ridge erosion or destruction by impact craters would similarly lead to single ridges being subdivided into short ridge segments with relatively high relief. Finally, single ridges are also seen to be subdivided into multiple segments in the tectonic catalog with no clear evidence of physical segmentation, suggesting that the existing database of tectonic landforms on Mercury is not optimized for displacement–length relationships. Using length-scaling relationships derived from individually mapped and well-separated ridges for ridges affected by these processes will significantly underestimate the displacement and hence, the tectonic strain. Moreover, although issues arising from real or apparent fault segmentation may average out in calculating average fault height globally (provided the displacement–length ratio is derived from a similar data set of ridges), since the two are linearly related, the total surface strain scales with the product of fault length and height and thus the square of fault length if a displacement–length ratio is used, leading to systematic biases in the resulting strain calculations.

Our ridge height measurements and associated displacements reveal that there is a large spread in apparent displacement–length ratios among Mercury's shortening landforms with numerous short ridges with high relief (Figure 6, see also Peterson et al., 2019). The spread is observed using either the maximum displacement along a ridge or using the average displacement from the average profile of the ridge. This trend can be partially affected by different fault populations with varying dip angles, but predominantly indicates that ridge segmentation in the catalogs affects both the high-relief ridge and lobate scarp database of Watters (2021) as well as the catalog of Klimczak et al. (2025). For that reason, a fit to this global cloud of points would be inappropriate to define a realistic displacement–length ratio. Instead, a better approach is to consider a lower envelope, which estimates a representative minimum ridge elevation as a function of length for those ridges least affected by real or apparent segmentation. In order to define this lower envelope, we performed a least-square fit using the first quartile of ridge heights and the associated average length, after having sampled the ridge population per length using 100 bins. While the minimum height per length bin could be viewed as a statistical outlier, choosing the first quartile of the distribution should better reflect the expected ridge height at a given length. This approach should yield a better estimate of the true displacement–length ratio if the real and apparent fault segmentation were taken into account. We note that power-law fits have also been constructed in the literature (with exponents close to 1; e.g. Loveless & Klimczak, 2025), but for simplicity we here only focus on the simple linear relationship. Because of the potentially important effect of ridge segmentation, we also force the linear fit to go through zero, in keeping with the traditional use of displacement-length ratios in previous studies.

Considering wrinkle ridges only and the average displacement along a ridge, we obtain a best-fit lower envelope displacement–length ratio of 3.4×10^{-3} (6.0×10^{-3} for the lower envelope of the maximum displacement). A similar ratio of 3.4×10^{-3} (5.8×10^{-3} for the lower envelope of the maximum displacement) is obtained for high-relief ridges and lobate scarps. Ratios that consider the average displacement along a ridge subsegment are about two times lower than scaling relationships, using the maximum displacement, which have been derived and used in previous work (7.2×10^{-3} in Watters, 2021; 8.1×10^{-3} in Byrne et al., 2014). In comparison, using the maximum displacement along a ridge, rather than the average, would drastically lower this difference (~10%–25% lower).

Our mapping can further help address the suitability of using displacement–length ratio with this data set and using maximum versus average ridge height, in comparison to using the measured average ridge height for each feature, when estimating global strain (Table 1). Using a 7.2 or 8.1×10^{-3} (Byrne et al., 2014; Watters, 2021) scaling ratio rather than the measured displacement for each fault underestimates global strain by about 30% and 15%, respectively. This effect is due to ridge segmentation and the square of ridge length affecting strain estimates using displacement–length ratios. Using the maximum height rather than considering the local variability in ridge height and associated fault displacement leads to an overestimation of global contraction by about 50% in all cases. For these reasons, all upcoming sections do not rely on displacement–length ratios, but make use of the locally estimated landform height to infer the displacement and strain.

Table 1
Comparison of Average Global Linear Strain Estimates From the Tectonic Record for Different Approaches

Linear strain (%)	All ridges[a]	Lobate scarps[b]	High-relief ridges[b]	Wrinkle ridges[a]
7.2×10^{-3} scaling	0.413	0.074	0.012	0.241
8.1×10^{-3} scaling	0.465	0.084	0.014	0.271
Using the maximum estimated height for each ridge	0.820	0.131	0.017	0.568
Using the measured height for each ridge subsegment	**0.537**	**0.087**	**0.012**	**0.378**

Note. The assumed fault dip is 30°. The last row in bold is our preferred mapping approach that estimates the ridge height for each ridge subsegment. Note that this maximum linear strain estimate doesn't account for ridge azimuth as discussed in Section 2.6. For all ridges and wrinkle ridges, we use the mapping of Klimczak et al. (2025), while lobate scarps and high-relief ridges are from Watters (2021). As both tectonic databases are not identical, the 3 last columns may not add up to the first. [a]from the tectonic catalog of Klimczak et al. (2025). [b]from the tectonic catalog of Watters (2021).

3.4. Tectonic Strain and Global Contraction

As discussed in Section 2.5, the selection of primary ridges and exclusion of adjacent related structures can prominently affect tectonic strain. For that reason, we here present two tectonic strain maps (Figure 7), one considering all ridge segments mapped in Klimczak et al. (2025), and a second considering only our primary ridge mapping assuming our preferred parameters ($W = 50$ km, $A = 30°$, $O = 20\%$). For clarity, we start by providing some average global contraction values using our tectonic strain mapping and then show and discuss laterally variable strain values.

Our first strain map (Figures 7a and 7b) considers that all shortening landforms are associated with an individual fault whose displacement is represented by the relief of the overlying ridge, not excluding nearby adjacent structures. We note that all calculations presented below assume a constant fault dip angle of 30°. For this model, we obtain an average global strain of $3.4 \pm 1.8 \times 10^{-3}$ and contraction of 8.3 ± 4.5 km. Considering only the cratered plains, we find a strain of $3.3 \pm 1.7 \times 10^{-3}$ and contraction of 8.1 ± 4.4 km, and for the smooth plains, we find a strain of $3.8 \pm 1.9 \times 10^{-3}$ and contraction of 9.2 ± 4.7 km. These results are generally consistent with

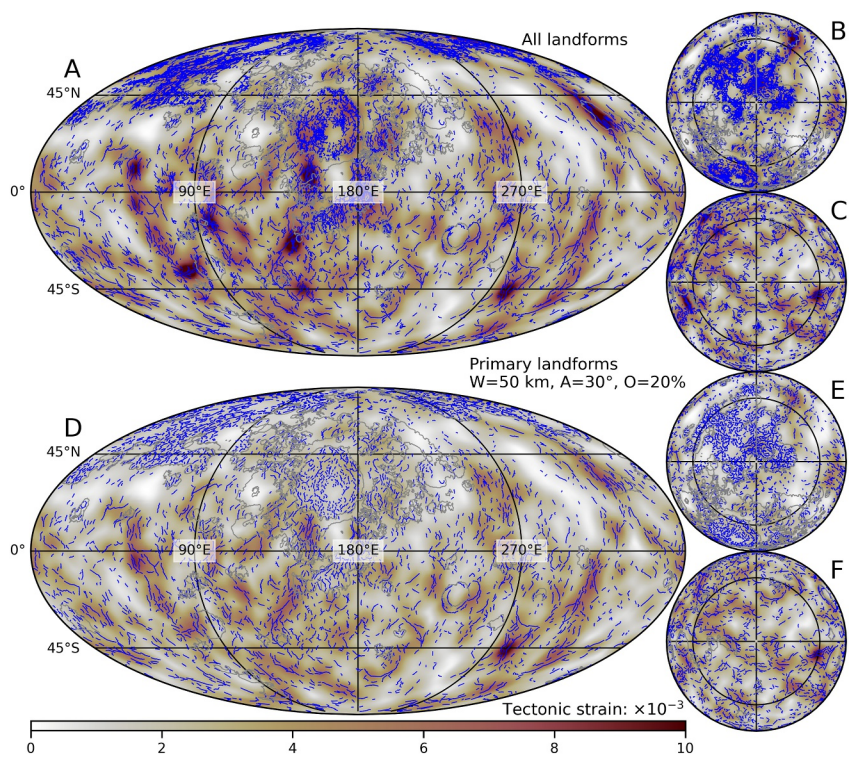

Figure 7. Tectonic strain as mapped considering all landforms (a, b) and only primary (c, d) landforms using the same format as Figure 1. A map without the annotated landforms is provided in Figure S8 in Supporting Information S1.

Table 2
Area-Weighted Mean and Standard Deviation of Global Contraction and Tectonic Strain for Different Models and Assuming a 30° Dip

	All landforms		Primary landforms	
	Global contraction (km)	Strain ($\times 10^{-3}$)	Global contraction (km)	Strain ($\times 10^{-3}$)
Global	8.3 ± 4.5	3.4 ± 1.8	6.3 ± 3.2	2.6 ± 1.3
Cratered terrain	8.1 ± 4.4	3.3 ± 1.7	6.6 ± 3.3	2.7 ± 1.4
Smooth plains	9.2 ± 4.7	3.8 ± 1.9	5.3 ± 2.5	2.2 ± 1.0
Northern hemisphere	7.6 ± 4.5	3.1 ± 1.8	5.3 ± 2.8	2.2 ± 1.2
Southern hemisphere	9.0 ± 4.3	3.7 ± 1.8	7.4 ± 3.2	3.0 ± 1.3
Eastern hemisphere	7.6 ± 4.2	3.1 ± 1.7	6.2 ± 3.3	2.5 ± 1.3
Western hemisphere	9.0 ± 4.5	3.7 ± 1.9	6.5 ± 3.2	2.6 ± 1.2

Note. Both tectonic maps are shown in Figure 7.

previous work (Byrne et al., 2014; Crane & Klimczak et al., 2019b; Table 2). The 1-σ ranges reflect the spatial variability in the strain on scales larger than the 400-km averaging window used in generating the strain map, which is likely introduced by regional geodynamics. We note that the values overlap at the 1-σ level, which implies similar strains between the cratered terrains and smooth plains (see also Peterson et al., 2019). This result indicates that the density of tectonic structures alone, which is greater in the smooth plains, is not a good indicator of strain. In the smooth plains, landforms might be associated with a shallower dip angle (Loveless et al., 2025), implying that our model may slightly underestimate strain there. We interpret the lack of a pronounced strain excess in the smooth plains to result from their reduced height and more disorganized distribution compared with lobate scarps and high-relief ridges.

Our tectonic strain map further shows important north–south trending bands exceeding strains of $\sim 8.0 \times 10^{-3}$ (see also Watters et al., 2021). These high strain regions are in contrast to areas showing a prominent strain deficit with strain $<0.4 \times 10^{-3}$, which are located east and west of the Caloris basin on a 30°–60°N latitudinal band. Some of the low-strain regions correspond to younger craters and basins, such as the Raditladi (120°E, 27°N) and Rachmaninoff basins (60°E, 28°N), that have erased any pre-existing geology. Thus, the strain map does not adequately reflect strain pre-dating the age of the surface. We address the evolution of strain through time below. In this map, strain recorded in the northern hemisphere ($3.1 \pm 1.8 \times 10^{-3}$) is slightly lower than, though overlapping at the 1-σ level with, that in the southern hemisphere ($3.7 \pm 1.8 \times 10^{-3}$).

We note that considering only high-relief ridges and lobate scarps and neglecting ridge distribution, our model constrains contraction to be near-zero where they are absent in the northern smooth plains, and to be about 4 km in the southern hemisphere, with a global average of 1.2 km, which is consistent with Watters (2021). However, and as discussed below, many isolated wrinkle ridges cannot be linked to a large primary lobate scarp or high-relief ridge. As shown in our companion paper (Broquet & Andrews-Hanna, 2026), many wrinkle ridges also cannot be explained by lithospheric loading using present-day gravity and topography data. As a result, ignoring wrinkle ridges leads to an important underestimation of global contraction.

The second map (Figures 7c and 7d) was constructed using only our estimated primary landforms. This approach acknowledges the fact that the fault database sometimes includes segments that are closely parallel to or on the flanks of larger ridges that are also in the database, which leads to double counting of strain in our calculations. Similarly, two parallel structures could in some cases be related to a single dominant fault at depth. The tectonic strain map constructed using only our estimated primary landforms displays an overall strain reduction by ~20% compared to the map discussed above, with a global strain of $2.6 \pm 1.3 \times 10^{-3}$ and global contraction of 6.3 ± 3.2 km (see Table 2). Notably, even in this conservative case, the global contraction recorded in the cratered terrain of 6.6 km is markedly higher than the ~1.2 km of global contraction estimated when neglecting wrinkle ridges (Watters, 2021). As for the case using all ridges, the strain recorded in the cratered terrains ($2.7 \pm 1.4 \times 10^{-3}$) and in the smooth plains ($2.3 \pm 1.0 \times 10^{-3}$) are roughly similar. As in the map considering all ridges, strain in the northern hemisphere ($2.2 \pm 1.2 \times 10^{-3}$) is lower though it strongly overlaps at the 1-σ level of

contraction in the southern hemisphere ($3.0 \pm 1.3 \times 10^{-3}$). This north–south difference is due to the southern hemisphere hosting more lobate scarps.

This more conservative strain mapping resulted in significant reductions of strain in some areas of dense faulting. As an example, while the northern smooth plains and the Caloris region displayed high strain considering all landforms, selecting only primary faults turned these regions to local strain lows when compared to regions covered by lobate scarps (Figure 7). We consider this second map to provide a more conservative endmember to discuss Mercury's global contraction. For comparison, we also provide in Table S1 in Supporting Information S1, contraction values for different assumed parameters for the selection of primary landforms.

As noted in the previous sections, a few additional parameters affect the ridge heights and tectonic strains inferred using our automatic ridge extraction approach. These include the maximum allowed offset between the mapped tectonic segment and the ridge delimitation (in case the segment doesn't perfectly overlap with the ridge), the boxcar processing of the network's inferred probability of belonging to the ridge, and the size of the moving window. The first two parameters only moderately affect global contraction estimates (±1 km). Decreasing the investigation window size increases tectonic strain and global contraction, as less area is allowed to release strain in the direction perpendicular to the main strain component. For the case of a small investigation window encompassing a single ridge, e_2 will be equal to zero and the total strain will increase. Using investigation windows of 200 and 600 km instead of 400 km respectively increased and decreased our global contraction estimates to 7.6–5.3 km (as compared to our nominal value of 6.3 km).

4. Discussion

4.1. Compressional Strains Maintained by the Brittle Strength of Mercury's Lithosphere

Planetary lithospheres can sustain non-negligible elastic strains before inelastic deformation occurs, including brittle failure and faulting (e.g., Goetze & Evans, 1979). Work by Klimczak (2015) estimated the strength of Mercury's fractured upper crust and calculated that up to 2 km of radial contraction might have been stored at depths of 30 m before failure (and up to ~6 km if the upper crust were fully intact, which was deemed unlikely). However, the pervasive faulting on Mercury clearly shows that the failure criteria have been exceeded, and any early pre-faulting strain buildup would have been released during the subsequent tectonism. Thus, any strain stored in the lithosphere prior to failure should not be added to the tectonic inventory of strain. Nevertheless, even for a faulted planetary lithosphere, substantial stress can be maintained in the lithosphere by friction, as governed by Byerlee's rule (Brace & Kohlstedt, 1980; Byerlee, 1978; Kohlstedt & Mackwell, 2010). The frictional strength of the lithosphere scales linearly with pressure and depth. Using Byerlee's intermediate- and high-pressure laws at depths of 1–10 km, the frictional stress and strain that can be maintained in Mercury's lithosphere correspond to a radius change of about 1–13 km, considering a bulk density of 2,700 kg m^{-3}, a Poisson's ratio of 0.25, and a Young's modulus of 73 GPa.

Although large amounts of strain can in theory be stored elastically at modest depths due to the lithosphere's frictional strength, faults forming in the upper lithosphere can propagate to deeper levels due to the focusing of stress at the propagating fault tips (e.g., Scholz, 2019). Since the strain that is accommodated elastically at greater depths must be accommodated by fault displacement at shallow depths, it is not clear to what extent this affects the fidelity of the tectonic record of strain. Nevertheless, it must be acknowledged that the tectonic strain is a lower bound on the actual amount of strain the lithosphere has undergone over time.

Finally, planets may also experience an early phase of global expansion related to internal heating (e.g., Tosi et al., 2013). Depending on when the crust crystalizes, it would either form stress-free on a globally expanded planet or store a record of this early expansion phase in its tensile strain record. On the Moon, evidence of ancient igneous intrusions indicates that the bulk of the crust recorded this global expansion phase (Andrews-Hanna et al., 2013). Therefore, before planetary contraction starts to be expressed in the tectonic record, strains may need to overcome any pre-existing extension as well as the compressive yield strength of the crust.

4.2. Time Evolution of Tectonic Strain

For a simple scenario of global cooling, older surfaces should accumulate more tectonic strain. However, this pattern is not always observed, as is the case for the southern highlands of Mars, where older regions show an apparent strain deficit relative to adjacent smooth plains (Andrews-Hanna & Broquet, 2023). This apparent

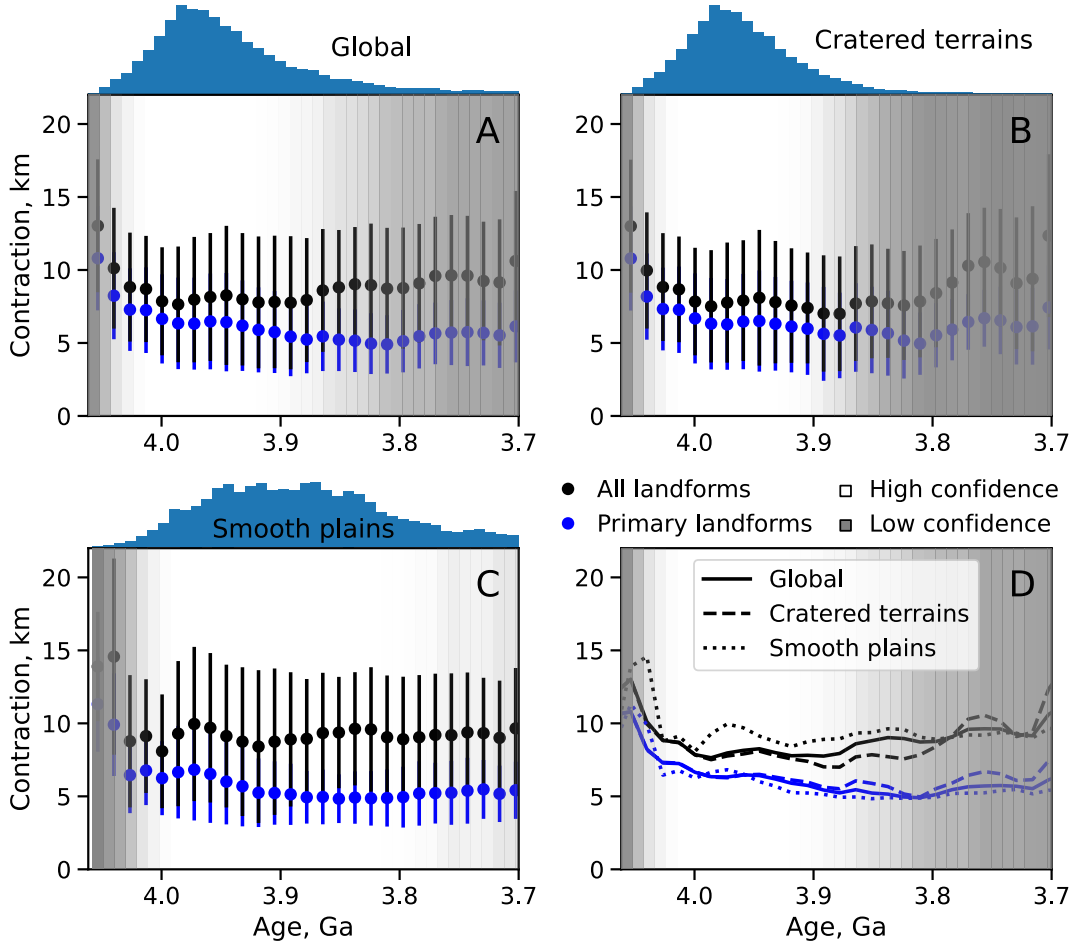

Figure 8. Planetary contraction versus time globally (a), in the cratered terrains (b) and in regions covered by smooth plains (c), as well as altogether (d). Surface age is estimated from N(20) and using the model of Neukum et al. (2001). A plot with the chronology model of Le Feuvre and Wieczorek (2011) is shown in Figure S9 in Supporting Information S1. The vertical bar denotes the standard deviation to the mean and the gray shade indicates our relative confidence in the contraction estimation given the areal fraction of surfaces with specific ages. Histograms are appended to the *x*-axis and show the areal fraction for each age bin. Given the small areal fraction of surfaces with ages <3.8 or >4.1 Ga, contraction estimates in these regions are deemed highly uncertain.

discrepancy reflects either the incompleteness of the ancient contractional tectonic record of strain, or the accommodation of strain by means other than large-scale tectonism (Andrews-Hanna & Broquet, 2023; Broquet & Andrews-Hanna, 2023).

Here, we make use of crater counting statistics to infer the relationship between surface age and tectonic strain on Mercury. Surface age is estimated by counting craters with diameter greater than 20 km (Herrick et al., 2018) within a 400-km wide moving window and using the chronology model of Neukum et al. (2001). Local surface age is then compared to local tectonic strain and estimated contraction (Figure 8). We note that other production and chronology functions accounting for different orbital and impact parameters have been proposed (e.g., Le Feuvre & Wieczorek, 2011). From the same N(20) population, the predicted absolute age can often differ by more than 200 Myrs, depending on the input model (see Orgel et al., 2020). For that reason, we also provide a contraction history using the Le Feuvre and Wieczorek (2011) parameters in Figure S9 in Supporting Information S1. This latter model does not affect the relative strain and contractional history but does change the absolute model age. For example, the Neukum et al. (2001) parameters predict smooth plain and cratered terrain ages of ~3.9–4.0 Ga, compared to 3.7–3.8 Ga for the Le Feuvre and Wieczorek (2011) non-porous model (see also Wang et al., 2021). Importantly, our analysis does not assign an absolute age to the deformation but, by superposition, it necessitates the deformation to postdate the age of the surface. Thus, relative strain differences

between two different aged terrains can be used to infer a strain history. We note that as we are using a large, 400-km wide, investigation window, our age estimates are not sensitive to the floor of small-scale craters that might crosscut and postdate the formation of a fault. Instead, our crater counting approach is sensitive to the age of the large-scale crustal block that the fault formed into and natural postdates.

This figure reveals that the expected relationship between older surface age and higher global contraction is generally expressed when considering primary tectonic landforms. Including all landforms results in greater values of global contraction recorded on younger surfaces than on older surfaces, which supports our use of the primary structures for the strain inventory. We further find no prominent difference between the time-history of global contraction in the smooth plains and cratered terrains. Although the standard deviations are somewhat large, reflecting the spatially heterogeneous tectonic fabric of Mercury, the general tendency shows a relatively rapid ∼4 km decrease in planetary radius after crustal formation from ∼4.1 to 4.0 Ga (or 3.9 to 3.8 Ga for the chronology model of Le Feuvre & Wieczorek, 2011; Figure S9 in Supporting Information S1) at a rate of ∼0.04 km/Myr (or 40 km/Gyr) for all investigated regions, though the oldest surfaces are less abundant and the corresponding strain less certain. From 4.0 to 3.9 Ga, this rate decreases to about 0.01 km/Myr, then flattens out through 3.7 Ga. These results are generally consistent with Crane and Klimczak (2017), who also showed a non-steady contraction history, though that work only focused on the northern smooth plains. The strain history of Mars is similarly uneven (Andrews-Hanna & Broquet, 2023), with a large rate of radial contraction during the short interval of the early Hesperian (0.02–0.05 km/Myr from 3.57 to 3.40 Ga) and a much lower rate of contraction (2×10^{-4}–4×10^{-4} km/Myr or 0.2–0.4 km/Gyr since 3.4 Ga). On Mars, this high rate of contraction may be related to the volcanic outpourings that formed the Hesperian-aged volcanic plains and associated changes in internal geodynamics.

Given the low abundance of terrains on Mercury with ages <3.8 Ga or >4.05 Ga, we deem our contraction estimates for these periods highly uncertain. All analyses show ∼5 km of global contraction recorded on even the youngest surfaces, which must have accumulated since 3.7 Ga at an average rate of ∼1.35 km/Gyr. This average rate of contraction over most of Mercury's history is more than an order of magnitude lower than the rate recorded on the oldest surfaces. This late contraction may not have been evenly distributed over this time interval, with higher rates earlier and lower rates today being likely considering the much higher rate of strain in Mercury's earliest history.

Mercury's earliest thermal history is associated with radiogenic heating, core crystallization, interior melting and crustal formation, which can lead to global warming and net planetary expansion (Grott et al., 2011; Tosi et al., 2013). The expected phase of global expansion is predicted to last until ∼3.9 Ga (Tosi et al., 2025), which is in contrast to our observed peak in global contraction. However, we note that the estimated expansion due to crust production and its contribution to the net radius change depends on many unknown parameters, including the interior thermal conductivity and expansivity (see also Davies et al., 2024; Knibbe & van Westrenen, 2018). The change in contraction rate indicates that Mercury's early history (∼4.1–4.0 Ga) might be related to some change in global geodynamics at that time, leading to a substantial contraction of the interior. This high strain period overlaps with the formation of the inter-crater plains and the early phases of smooth plains volcanism, and could be associated with changes in internal dynamics and the extraction of melt leading to volcanism (Head et al., 2011; Marchi et al., 2013). An early despinning event could have led to the record of a substantial and temporally distinct contraction event leading to the formation of the north–south oriented tectonic strain bands (Matsuyama & Nimmo, 2009, see also Figure 7). An early high strain period followed by slower rates could also mark the onset of inner core growth, as the associated release of latent heat would slow contraction rates (e.g., Dumberry & Rivoldini, 2015).

4.3. The In-Development Mercatss Catalog

An updated tectonic catalog (MerCatSS, Bernhardt et al., 2025) is currently being developed, in which an additional cumulative total of ∼100,000 km of shortening landforms have been identified with a high degree of certainty. Importantly, these newly identified landforms generally have the same spatial distribution as the features of the Klimczak et al. (2025) catalog used in this work (Figure S9 in Supporting Information S1). They further have smaller lengths (∼40 vs. ∼65 km) and estimated heights (∼330 vs. ∼460 m) compared to other similar landforms in the Klimczak et al. data set. Finally, with our primary ridge selection approach, a large fraction of these newly mapped features would likely be removed. For these reasons, the general conclusions on

the distribution and time evolution of tectonic strain and contraction determined in this work would not be substantially affected by using this updated catalog.

5. Conclusion

We have re-evaluated Mercury's tectonic history using global tectonic databases, a global DEM, and a machine learning algorithm to evaluate tectonic shortening from direct measurements, taking into account overlapping structures and the orientations of features. Our neural network can be used to extract the end point of a tectonic landform from an elevation profile orthogonal to the strike. From the ridge end points, it is straightforward to estimate ridge parameters, and this was here applied to determine the heights of 53,085 ridge subsegments derived from a global database of tectonic features. This approach improves upon prior studies that relied on scaling ratios to infer ridge height from length and allows a robust estimation of tectonic strain that better accounts for ridge segmentation, incomplete mapping, as well as for the variability in ridge height along a given tectonic landform. We have developed an approach to avoid double counting of strain in cases where multiple ridge segments are linked to a single large fault at depth. This primary ridge mapping is deemed to provide a better estimate of global contraction for Mercury when using the global tectonic catalog of Klimczak et al. (2025). Finally, we have proposed a formulation to estimate global contraction by considering the orientation and distribution of faults, which improves upon previous work that implicitly assumed the tectonic landforms to be randomly organized.

Our best-fit, length-averaged, lower envelope displacement–length ratios for the database of Klimczak et al. (2025) are similar for wrinkle ridges, lobate scarps and high-relief ridges, with a value of 3.4×10^{-3}. This value is about two times lower than that found in previous work ($7–8 \times 10^{-3}$ Byrne et al., 2014; Watters, 2021). Higher ratios were obtained in previous work as these typically focused on the maximum displacement rather than the average and on a few unsegmented ridges. However, our work demonstrates that although the fault displacement–length proportionality is a robust phenomenon rooted in the physics of elasticity and fault growth, such ratios cannot be reliably applied to global tectonic databases that are not adequately tailored for such use and in which long ridges are segmented by geologic or mapping means. Indeed, classical displacement–length ratios ($7–8 \times 10^{-3}$) led to the systematic underestimation of strain and global contraction, by 15% and up to 30%.

While using all tectonic features may overestimate strain because of overlapping ridges connected to a single fault at depth, ignoring wrinkle ridges underestimates the strain. Considering primary landforms, we estimate Mercury's global contraction to be 6.3 km, as displayed in the tectonic record, with no significant difference between the cratered terrains and smooth plains at the 1-σ level. This value is considerably higher than previous work that neglected wrinkle ridges (~1.2 km), while avoiding double counting of nearby ridges (Watters et al., 2021). The similar strains recorded in smooth plains and cratered terrains indicate that wrinkle ridges have recorded a substantial amount of global contraction and cannot be neglected when investigating Mercury's global cooling history. The total accumulated strain may be higher given that we here used a smoothed DEM, and because a non-negligible fraction of strain from planetary contraction might have been accommodated by non-tectonic means. Finally, varying the assumed fault dip angle from 30° to 25–35° would affect the inferred global contraction by about 20%, with shallower dips requiring higher contraction.

From crater counting statistics, our tectonic strain history indicates a period of rapid contraction from 4.1 to 3.9 Ga at rates of 0.02–0.04 km/Myr, followed by much lower rates of contraction, which has implications for Mercury's geodynamic history. This strain history is remarkably similar to that of Mars, which experienced a similar pulse of contraction at a somewhat later time during the early Hesperian (3.57–3.40 Ga, Andrews-Hanna & Broquet, 2023). On both planets, the high rates of strain may be associated with volcanic outpourings and associated internal geodynamics. The drastic reduction in contraction rate after 3.9 Ga could also mark the onset of inner core nucleation (e.g., Dumberry & Rivoldini, 2015), the timing of which is possibly supported by similarly aged strong remnant magnetic anomalies preserved in the crust (Johnson et al., 2015).

Lateral variations in tectonic strain can help reveal the geodynamic history of Mercury. Locally, tectonic strain and shortening exhibit prominent lateral variations, with some regions experiencing near-zero strain, while others recorded strains of $\sim 8 \times 10^{-3}$. Such tectonic strain variations might be linked to local geodynamic events, including plume-induced flood volcanism sequences and lithospheric loading (e.g., Andrews-Hanna & Broquet, 2023; Broquet & Andrews-Hanna, 2023). Variable crustal heat production or volcanic heat transfer could also affect tectonic strain and contraction (Peterson et al., 2021).

In our second companion paper (Broquet & Andrews-Hanna, 2026), we discuss how membrane–flexural strains as inverted from gravity and topography contribute to the tectonic record. We demonstrate that the predicted membrane–flexural strains show magnitudes similar to the tectonic strain and can explain some of the spatial variability in tectonic strain. That study further shows that regional membrane–flexural strain can counteract contractional strain as well as add to it. Thus, the global mean strain and associated contraction are not affected by local lithospheric deformations, implying that the general conclusions of the present-work hold.

Conflict of Interest

The authors declare no conflicts of interest relevant to this study.

Availability Statement

Mercury's global DEM is available at the USGS Astrogeology website (https://astrogeology.usgs.gov/) and the tectonic map is available at Klimczak et al. (2024). The Neural Network model was designed with TensorFlow version 2.19.0 (Abadi et al., 2016). The Neural Network training set, our tectonic database that includes ridge height and class, together with our strain maps, is available at Broquet (2025).

Acknowledgments

This work was supported by a Alexander von Humboldt grant and an Emmy Noether Junior Group Leader grant from DFG to AB, as well as an augmentation from the NASA Discovery Data Analysis Program to NASA Lunar Data Analysis Program Grant 80NSSC22K1340 to JCAH. AB thanks Gaku Nishiyama and Nicola Tosi for the interesting discussions about Mercury's tectonic record and radial contraction. We thank Stefan Loveless and Christian Klimczak for providing feedback on an earlier version of this manuscript. Open Access funding enabled and organized by Projekt DEAL.

References

Abadi, M., Barham, P., Chen, J., Chen, Z., Davis, A., Dean, J., et al. (2016). TensorFlow: A system for large-scale machine learning. In *Proceedings of the 12th USENIX conference* (pp. 265–283). https://doi.org/10.5555/3026877.3026899

Allemand, P., & Thomas, P. (1995). Localization of Martian ridges by impact craters: Mechanical and chronological implications. *Journal of Geophysical Research*, *100*(E2), 3251–3262. https://doi.org/10.1029/94JE03081

Andrews-Hanna, J. C. (2020). The tectonic architecture of wrinkle ridges on Mars. *Icarus*, *351*, 113937. https://doi.org/10.1016/j.icarus.2020.113937

Andrews-Hanna, J. C., Asmar, S. W., Head, J. W., Kiefer, W. S., Konopliv, A. S., Lemoine, F. G., et al. (2013). Ancient igneous intrusions and early expansion of the Moon revealed by GRAIL gravity gradiometry. *Science*, *339*(6120), 675–678. https://doi.org/10.1126/science.1231753

Andrews-Hanna, J. C., & Broquet, A. (2023). The history of global strain and geodynamics on Mars. *Icarus*, *395*, 115476. https://doi.org/10.1016/j.icarus.2023.115476

Becker, K. J., Robinson, M. S., Becker, T. L., Weller, L. A., Edmundson, K. L., Neumann, G. A., et al. (2016). First global digital elevation model of Mercury. In *47th lunar and planetary science conference* (p. 2959).

Bernhardt, H., Clark, J. D., Crane, K. T., Preusker, F., Klimczak, C., Banks, M. E., et al. (2025). The Mercury catalog of shortening structures (MerCatSS): The most complete and accurate tectonic map of Mercury. In *EPSC-DPS joint meeting 2025*. EPSC-DPS2025-2108. https://doi.org/10.5194/epsc-dps2025-2108

Beuthe, M. (2010). East–west faults due to planetary contraction. *Icarus*, *209*(2), 795–817. https://doi.org/10.1016/j.icarus.2010.04.019

Brace, W. F., & Kohlstedt, D. L. (1980). Limits on lithospheric stress imposed by laboratory experiments. *Journal of Geophysical Research*, *85*(B11), 6248–6252. https://doi.org/10.1029/JB085iB11p06248

Broquet, A. (2025). Data for Mercury's tectonic and geodynamic history [Dataset]. *Zenodo*. https://doi.org/10.5281/zenodo.15234776

Broquet, A., & Andrews-Hanna, J. C. (2023). Plume-induced flood basalts on Hesperian Mars: An investigation of Hesperia Planum. *Icarus*, *391*, 115338. https://doi.org/10.1016/j.icarus.2022.115338

Broquet, A., & Andrews-Hanna, J. C. (2026). Mercury's tectonic and geodynamic history: 2. Contribution of membrane–flexural strains to the tectonic record. *Journal of Geophysical Research: Planets*, *131*, e2025JE009585. https://doi.org/10.1029/2025JE009585

Byerlee, J. D. (1978). Friction of rocks. *Pure and Applied Geophysics*, *116*(4–5), 615–626. https://doi.org/10.1007/BF00876528

Byrne, P. K., Klimczak, C., Celâl Şengör, A., Solomon, S. C., Watters, T. R., & Hauck II, S. A. (2014). Mercury's global contraction much greater than earlier estimates. *Nature Geoscience*, *7*(4), 301–307. https://doi.org/10.1038/ngeo2097

Byrne, P. K., Klimczak, C., & Şengör, A. M. C. (2018). The tectonic character of Mercury. In S. C. Solomon, L. R. Nittler, & B. J. Anderson (Eds.), *Mercury: The view after MESSENGER*, (pp. 249–286). Cambridge Planetary Science

Cartwright, J. A., Trudgill, B. D., & Mansfield, C. S. (1995). Fault growth by segment linkage: An explanation for scatter in maximum displacement and trace length data from the Canyonlands Grabens of SE Utah. *Journal of Structural Geology*, *17*(9), 1319–1326. https://doi.org/10.1016/0191-8141(95)00033-A

Crane, K. T., & Klimczak, C. (2017). Timing and rate of global contraction on Mercury. *Geophysical Research Letters*, *44*(7), 3082–3089. https://doi.org/10.1002/2017GL072711

Crane, K. T., & Klimczak, C. (2019a). A 3-D structural model of the Saddle Mountains, Yakima Fold Province, Washington, USA: Implications for late Tertiary tectonic evolution of the Columbia River Flood Basalt Province. *Tectonophysics*, *766*, 1–13. https://doi.org/10.1016/j.tecto.2019.05.015

Crane, K. T., & Klimczak, C. (2019b). Tectonic patterns of shortening landforms in mercury's Northern smooth plains. *Icarus*, *317*, 66–80. https://doi.org/10.1016/j.icarus.2018.05.034

Davies, C. J., Pommier, A., Greenwood, S., & Wilson, A. (2024). Thermal and magnetic evolution of Mercury with a layered Fe-Si(-S) core. *Earth and Planetary Science Letters*, *641*, 118812. https://doi.org/10.1016/j.epsl.2024.118812

Denevi, B. W., Ernst, C. M., Meyer, H. M., Robinson, M. S., Murchie, S. L., Whitten, J. L., et al. (2013). The distribution and origin of smooth plains on Mercury, J. *Geophys Research Planets*, *118*(5), 891–907. https://doi.org/10.1002/jgre.20075

Di Achille, G., Popa, C., Massironi, M., Mazzotta Epifani, E., Zusi, M., Cremonese, G., & Palumbo, P. (2012). Mercury's radius change estimates revisited using MESSENGER data. *Icarus*, *221*(1), 456–460. https://doi.org/10.1016/j.icarus.2012.07.005

Dombard, A. J., & Hauck II, S. A. (2008). Despinning plus global contraction and the orientation of lobate scarps on Mercury: Predictions for MESSENGER. *Icarus*, *198*(1), 274–276. https://doi.org/10.1016/j.icarus.2008.06.008

Dumberry, M., & Rivoldini, A. (2015). Mercury's inner core size and core-crystallization regime. *Icarus*, *248*, 254–268. https://doi.org/10.1016/j.icarus.2014.10.038

Freed, A. M., Blair, D. M., Watters, T. R., Klimczak, C., Byrne, P. K., Solomon, S. C., et al. (2012). On the origin of graben and ridges within and near volcanically buried craters and basins in Mercury's northern plains. *Journal of Geophysical Research*, *117*(E12), E00L06. https://doi.org/10.1029/2012JE004119

Galluzzi, V., Di Achille, G., Ferranti, L., Popa, C., & Palumbo, P. (2015). Faulted craters as indicators for thrust motions on Mercury. *Geological Society London, Special Publication*, *401*(1), 313–325. https://doi.org/10.1144/SP401.17

Galluzzi, V., Ferranti, M., Massironi, L., Giacomini, L., Guzzetta, L., & Palumbo, P. (2019). Structural analysis of the Victoria quadrangle fault systems on Mercury: Timing, geometries, kinematics, and relationship with the High-Mg Region. *Journal of Geophysical Research*, *124*(10), 2543–2562. https://doi.org/10.1029/2019JE005953

Goetze, C., & Evans, B. (1979). Stress and temperature in the bending lithosphere as constrained by experimental rock mechanics. *Geophysical Journal International*, *59*(3), 463–478. https://doi.org/10.1111/j.1365-246X.1979.tb02567.x

Grott, M., Breuer, D., & Laneuville, M. (2011). Thermo-chemical evolution and global contraction of Mercury. *EPSL*, *307*(1–2), 135–146. https://doi.org/10.1016/j.epsl.2011.04.040

Hardacre, K. M., & Cowie, P. A. (2003). Variability in fault size scaling due to rock strength heterogeneity: A finite element investigation. *Journal of Structural Geology*, *25*(10), 1735–1750. https://doi.org/10.1016/S0191-8141(02)00205-5

Hauck II, S. A., Dombard, A. J., Phillips, R. J., & Solomon, S. C. (2004). Internal and tectonic evolution of Mercury. *Earth and Planetary Science Letters*, *222*(3–4), 713–728. https://doi.org/10.1016/j.epsl.2004.03.037

Head, J. W., Chapman, C. R., Strom, R. G., Fassett, C. I., Denevi, B. W., Blewett, D. T., et al. (2011). Flood volcanism in the Northern high latitudes of Mercury revealed by MESSENGER. *Science*, *333*(6051), 1853–1856. https://doi.org/10.1126/science.1211997

Herrick, R. R., Bateman, E. M., & Bates, W. G. C. (2018). Observations from a global database of impact craters on Mercury with diameters greater than 5 km. *JGR: Planets*, *123*. https://doi.org/10.1029/2017JE005516

James, P. B., Zuber, M. T., Phillips, R. J., & Solomon, S. C. (2015). Support of long-wavelength topography on Mercury inferred from MESSENGER measurements of gravity and topography. *Journal of Geophysical Research: Planets*, *120*(2), 287–310. https://doi.org/10.1002/2014JE004713

Johnson, C. L., Phillips, R. J., Purucker, M. E., Anderson, B. J., Byrne, P. K., Denevi, B. W., et al. (2015). Low-altitude magnetic field measurements by MESSENGER reveal Mercury's ancient crustal field. *Science*, *348*(6237), 892–895. https://doi.org/10.1126/science.aaa8720

Karagoz, O., Kenkmann, T., & Wulf, G. (2022). Circum-Tharsis wrinkle ridges at Lunae Planum: Morphometry, formation, and crustal implications. *Icarus*, *374*, 114808. https://doi.org/10.1016/j.icarus.2021.114808

Kennedy, P. J., Freed, A. M., & Solomon, S. C. (2008). Mechanisms of faulting in and around Caloris basin, Mercury. *Journal of Geophysical Research*, *113*(E8), E08004. https://doi.org/10.1029/2007JE002992

Klimczak, C. (2015). Limits on the brittle strength of planetary lithospheres undergoing global contraction. *Journal of Geophysical Research: Planets*, *120*(12), 2135–2151. https://doi.org/10.1002/2015JE004851

Klimczak, C., Byrne, P. K., & Crane, K. (2024). *A global tectonic map of Mercury*. Mendeley Data, V2. https://doi.org/10.17632/p43b9wttpj.2

Klimczak, C., Byrne, P. K., & Crane, K. (2025). Mercury has multiple, superposed global tectonic patterns. *EPSL*, *658*, 119331. https://doi.org/10.1016/j.epsl.2025.119331

Klimczak, C., Watters, T. R., Ernst, C. M., Freed, A. M., Byrne, P. K., Solomon, S. C., et al. (2012). Deformation associated with ghost craters and basins in volcanic smooth plains on Mercury: Strain analysis and implications for plains evolution. *JGR: Planets*, *117*(E12), E00L03. https://doi.org/10.1029/2012JE004100

Knibbe, J. S., & van Westrenen, W. (2018). The thermal evolution of Mercury's Fe–Si core. *Earth and Planetary Science Letters*, *482*, 147–159. https://doi.org/10.1016/j.epsl.2017.11.006

Kohlstedt, D. L., & Mackwell, S. J. (2010). Strength and deformation of planetary lithospheres. In T. R. Watters & R. A. Schultz (Eds.), *Planetary tectonics* (pp. 397–456). Cambridge Univ. Press.

Krizhevsky, A., Sutskever, I., & Hinton, G. E. (2012). ImageNet classification with deep convolutional neural networks. *Advances in Neural Information Processing Systems*, *25*.

Le Feuvre, M., & Wieczorek, M. A. (2011). Nonuniform cratering of the Moon and a revised crater chronology of the inner Solar System. *Icarus*, *214*(1), 1–20. https://doi.org/10.1016/j.icarus.2011.03.010

Li, L., Jamieson, K., DeSalvo, G., Rostamizadeh, A., & Talwalkar, A. (2018). Hyperband: A novel bandit-based approach to hyperparameter optimization. *Journal of Machine Learning Research*, *18*, 1–52. https://doi.org/10.5555/3122009.3242042

Loveless, S. R., & Klimczak, C. (2025). Several kilometers of global contraction on Mercury: A sample-size independent assessment of fault strain. *AGU Advances*, *6*(4), e2025AV001715. https://doi.org/10.1029/2025AV001715

Loveless, S. R., Klimczak, C., Crane, K. T., & Byrne, P. K. (2025). Geometric forward modeling of thrust systems underlying shortening landforms on Mercury. *Journal of Structural Geology*, *198*, 105449. https://doi.org/10.1016/j.jsg.2025.105449

Loveless, S. R., Klimczak, C., McCullough, L. R., Crane, K. T., Holland, S. M., & Byrne, P. K. (2024). A statistical evaluation of the morphological variability of shortening landforms on Mercury. *Icarus*, *416*, 116106. https://doi.org/10.1016/j.icarus.2024.116106

MacQueen, J. (1967). Some methods for classification and analysis of multivariate observations. *Berkeley Symposium. on Mathematical. Statistics. and Probability.*, *5*(1), 281–297.

Mangold, N., Allemand, P., & Thomas, P. G. (1998). Wrinkle ridges of Mars: Structural analysis and evidence for shallow deformation controlled by ice-rich décollements. *Planetary and Space Science*, *46*(4), 345–356. https://doi.org/10.1016/S0032-0633(97)00195-5

Marchi, S., Chapman, C., Fassett, C., Head, J. W., Bottke, W. F., & Strom, R. G. (2013). Global resurfacing of Mercury 4.0–4.1 billion years ago by heavy bombardment and volcanism. *Nature*, *499*(7456), 59–61. https://doi.org/10.1038/nature12280

Matsuyama, I., & Nimmo, F. (2009). Gravity and tectonic patterns of Mercury: Effect of tidal deformation, spin-orbit resonance, nonzero eccentricity, despinning, and reorientation. *Journal of Geophysical Research*, *114*(E1), E01010. https://doi.org/10.1029/2008JE003252

Mège, D., & Riedel, S. P. (2001). A method for estimating 2D wrinkle ridge strain from application of fault displacement scaling to the Yakima folds, Washington. *Geophysical Research Letters*, *28*, 3545–3548. https://doi.org/10.1029/2001GL012934

Michel, N. C., Hauck II, S. A., Solomon, S. C., Phillips, R. J., Roberts, J. H., & Zuber, M. T. (2013). Thermal evolution of Mercury as constrained by MESSENGER observations. *Journal of Geophysical Research: Planets*, *118*(5), 1033–1044. https://doi.org/10.1002/jgre.20049

Montési, L. G. J., & Zuber, M. T. (2003). Clues to the lithospheric structure of Mars from wrinkle ridge sets and localization instability. *Journal of Geophysical Research*, *108*(E6). https://doi.org/10.1029/2002JE001974

Neukum, G., Ivanov, B., & Hartmann, W. (2001). Cratering records in the inner solar System in relation to the lunar reference System. *Space Science Reviews*, *96*(1–4), 55–86. https://doi.org/10.1023/A:1011989004263

Nishiyama, G., Preusker, F., Broquet, A., Stark, A., Hussmann, H., Hauber, E., & Tosi, N. (2026). First global map of Mercury's surface roughness down to kilometric baselines: Implications for the planet's geologic evolution. *The Planetary Science Journal*, *7*(3), 59. https://doi.org/10.3847/psj/ae447c

Okubo, C. H., & Schultz, R. A. (2004). Mechanical stratigraphy in the western equatorial region of Mars based on thrust fault–related fold topography and implications for near-surface volatile reservoirs. *GSA Bulletin*, *116*(5), 594–605. https://doi.org/10.1130/B25361.1

Orgel, C., Fassett, C. I., Michael, G., Riedel, C., van der Bogert, C. H., & Hiesinger, H. (2020). Re-examination of the population, stratigraphy, and sequence of Mercurian basins: Implications for Mercury's early impact history and comparison with the Moon. *JGR Planets*, *125*(8), e2019JE006212. https://doi.org/10.1029/2019JE006212

Pegg, D. L., Rothery, D. A., Conway, S. J., & Balme, M. R. (2021). A fault surface exposed on Mercury. *Planetary and Space Science*, *201*, 105223. https://doi.org/10.1016/j.pss.2021.105223

Peterson, G. A., Johnson, C. L., Byrne, P. K., & Phillips, R. J. (2019). Distribution of areal strain on Mercury: Insights into the interaction of volcanism and global contraction. *Geophysical Research Letters*, *46*(2), 608–615. https://doi.org/10.1029/2018GL080749

Peterson, G. A., Johnson, C. L., Byrne, P. K., & Phillips, R. J. (2020). Fault structure and origin of compressional tectonic features within the smooth plains on Mercury. *JGR: Planets*, *125*(7), e2019JE006183. https://doi.org/10.1029/2019JE006183

Peterson, G. A., Johnson, C. L., & Jellinek, A. M. (2021). Thermal evolution of Mercury with a volcanic heat-pipe flux: Reconciling early volcanism, tectonism, and magnetism. *Science Advances*, *7*(40), eabh2482. https://doi.org/10.1126/sciadv.abh2482

Rousseeuw, P. J. (1987). Silhouettes: A graphical aid to the interpretation and validation of cluster analysis. *Journal of Computational and Applied Mathematics*, *20*, 53–65. https://doi.org/10.1016/0377-0427(87)90125-7

Schleicher, L. S., Watters, T. R., Martin, A. J., & Banks, M. E. (2019). Wrinkle ridges on Mercury and the Moon within and outside of mascons. *Icarus*, *331*, 226–237. https://doi.org/10.1016/j.icarus.2019.04.013

Scholz, C. H. (2019). *The mechanics of earthquakes and faulting* (3rd ed.). Press. https://doi.org/10.1017/9781316681473.493.

Schultz, R. A. (1999). Understanding the process of faulting: Selected challenges and opportunities at the edge of the 21st century. *Journal of Structural Geology*, *21*(8–9), 985–993. https://doi.org/10.1016/S0191-8141(99)00025-5

Sibson, R. H., & Xie, G. (1998). Dip range for intracontinental reverse fault ruptures: Truth not stranger than friction? *Bulletin of the Seismological Society of America*, *88*(4), 1014–1022. https://doi.org/10.1785/BSSA0880041014

Tosi, N., Grott, M., Plesa, C., & Breuer, D. (2013). Thermochemical evolution of Mercury's interior. *Journal of Geophysical Research: Planets*, *118*(12), 2474–2487. https://doi.org/10.1002/jgre.20168

Tosi, N., Schulz, F., Walterová, M., & Padovan, S. (2025). The influence of spin–orbit resonances on the evolution of Mercury's mantle and crust. *Icarus*, *439*, 116630. https://doi.org/10.1016/j.icarus.2025.116630

Wang, Y., Xiao, Z., Chang, Y., Xu, R., & Cui, J. (2021). Short-term and global-wide effusive volcanism on Mercury around 3.7 Ga. *Geophysical Research Letters*, *48*(20), e2021GL094503. https://doi.org/10.1029/2021GL094503

Watters, T. R. (1988). Wrinkle ridge assemblages on the terrestrial planets. *Journal of Geophysical Research*, *93*(B9), 10236–10254. https://doi.org/10.1029/JB093iB09p10236

Watters, T. R. (2004b). Elastic dislocation modeling of wrinkle ridges on Mars. *Icarus*, *171*(2), 284–294. https://doi.org/10.1016/j.icarus.2004.05.024

Watters, T. R. (2021). A case for limited global contraction of Mercury. *Communications Earth & Environment*, *2*(1), 9. https://doi.org/10.1038/s43247-020-00076-5

Watters, T. R., James, P. B., & Selvans, M. M. (2021). Mercury's crustal thickness and contractional strain. *Geophysical Research Letters*, *48*(17), e2021GL093528. https://doi.org/10.1029/2021GL093528

Watters, T. R., Robinson, M. S., Bina, C. R., & Spudis, P. D. (2004). Thrust faults and the global contraction of Mercury. *Geophysical Research Letters*, *31*(4). https://doi.org/10.1029/2003GL019171

Zuber, M. T., Smith, D. E., Phillips, R. J., Solomon, S. C., Neumann, G. A., Hauck II, S. A., et al. (2012). Topography of the northern hemisphere of Mercury from MESSENGER laser altimetry. *Science*, *336*(6078), 217–220. https://doi.org/10.1126/science.1218805